APPENDIX A

METEOROLOGICAL MODELING FOR THE HGB ATTAINMENT DEMONSTRATION SIP REVISION FOR THE 2008 EIGHT-HOUR OZONE STANDARD

APPENDIX A: METEOROLOGICAL MODELING FOR THE HGB ATTAINMENT DEMONSTRATION SIP REVISION FOR THE 2008 EIGHT-HOUR OZONE STANDARD

Table of Contents

Appendix A i

Appendix A: Meteorological Modeling for the HGB Attainment Demonstration SIP Revision for the 2008 Eight-Hour Ozone Standard ii

1. Weather Research and Forecasting (WRF) Modeling Overview 1

2. WRF Preparation 5

   2.1 WRF Preprocessing System (WPS) 5

   2.2 WPS Quality Assurance 8

   2.3 WRF Model Configuration 11

3. WRF Model Performance Evaluation (MPE) Tools 12

   3.1 Observations 12

   3.2 Time Series Panels 14

   3.3 Scatter Plots 14

   3.4 WRF Cloud Fraction and GOES Cloud Fraction 16

   3.5 WRF Shortwave Radiative Flux and CAMS Shortwave Radiative Flux 18

4. WRF Modeling Performance 19

   4.1 May 2012 Episode Performance Evaluation 19

   4.2 June 2012 Episode Performance Evaluation 28

   4.3 June 2012 Episode Performance Evaluation of WRF SIP Configuration and Alternate WRF Configuration 36

   4.4 July 2012 Episode Performance Evaluation 43

   4.5 August 2012 HGB Episode Performance Evaluation 46

   4.6 September 2012 HGB Episode Performance Evaluation 56

   4.7 Conclusions 61

5. References 61

1. WEATHER RESEARCH AND FORECASTING (WRF) MODELING OVERVIEW

The Texas Commission on Environmental Quality (TCEQ) is using the WRF model version 3.7.1 to generate the meteorological inputs for the photochemical modeling supporting this State Implementation Plan (SIP) revision. The WRF modeling system was developed by a broad user community including the Air Force Weather Agency, national laboratories, and academia. Earlier TCEQ SIP modeling used the Fifth Generation Meteorological Model (MM5) developed jointly by the NCAR and the Pennsylvania State University (PSU). The TCEQ upgraded to the WRF model for the 2014 DFW Attainment Demonstration SIP revision. The present WRF modeling was conducted for the five months listed in Table 1-1: *HGB Meteorological 2012 Season*.

Table 1-1: HGB Meteorological 2012 Season

Episode	All Grids Begin Date/Time (UTC)	All Grids End Date/Time (UTC)
2012 Season	April 15, 2012 00:00	October 2, 2012 00:00

A Lambert Conformal Conic (LCC) map projection with geographical coordinates defined in Table 1-2: *Lambert Conformal Map Projections* was used for the WRF modeling.

Table 1-2: Lambert Conformal Map Projections

First True Latitude (Alpha):	33°N
Second True Latitude (Beta):	45°N
Central Longitude (Gamma):	97°W
Projection Origin:	97°W, 40°N
Spheroid:	Perfect Sphere, Radius = 6370 km

WRF was configured with two outer domains (36 kilometer (km) and 12 km horizontal grid resolution) with two-way nesting that cover the United States (U.S.) and south central portion of the country. A 4 km fine grid domain covering the eastern half of Texas is created with one-way nesting to focus on metropolitan areas with air quality degradation. Figure 1-1: *WRF Modeling Domains* shows the WRF nested domain configuration. Each WRF grid embeds a corresponding CAMx grid of the same horizontal resolution. The easting and northing ranges for each grid in the LCC projection are defined in Table 1-3: *WRF Modeling Domain Definitions* in units of km.

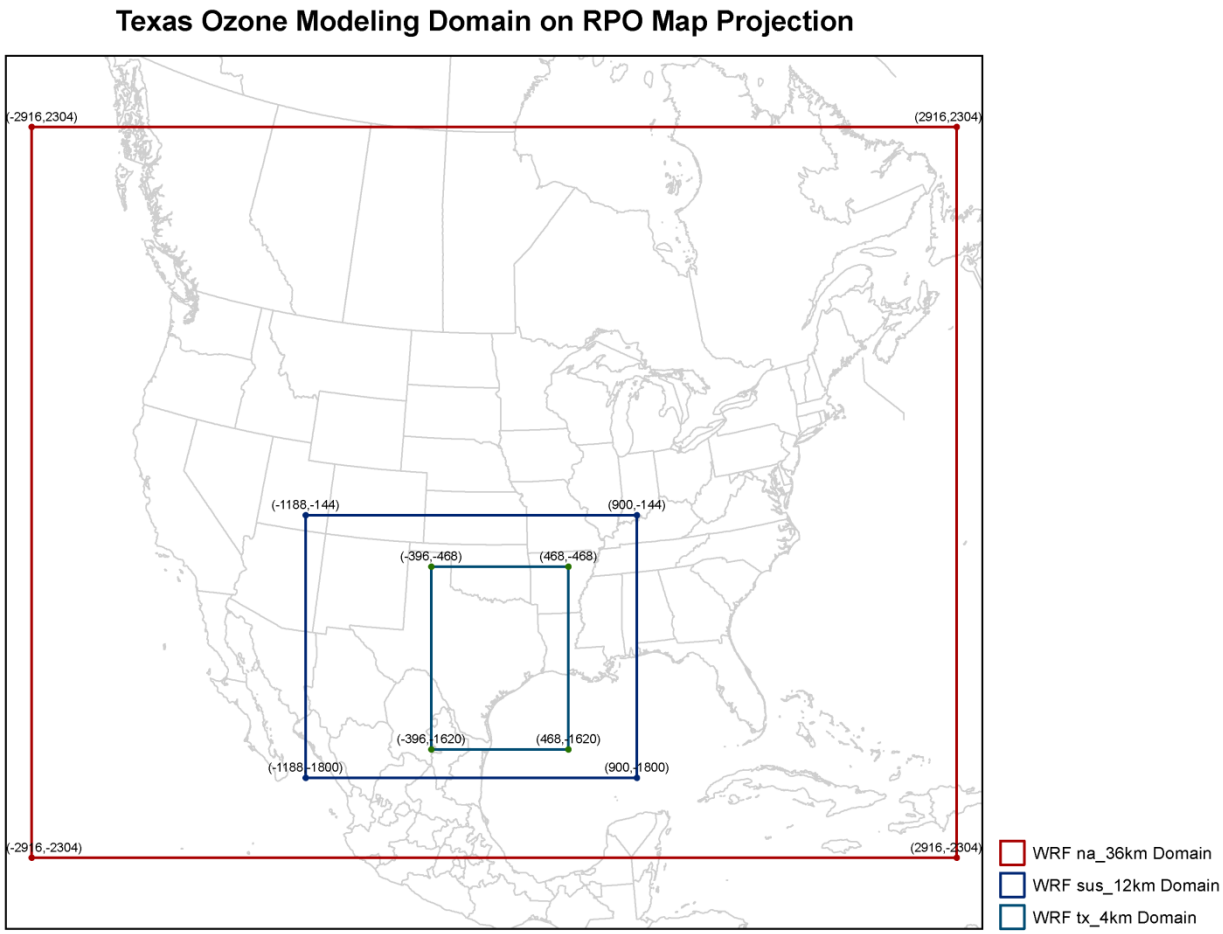

Figure 1-1: WRF Modeling Domains

Table 1-3: WRF Modeling Domain Definitions

Domain	Easting Range (km)	Northing Range (km)	East/West Grid Points	North/South Grid Points
36 km	(-2916,2916)	(-2304,2304)	163	129
12 km	-1188,900)	(-1800,-144)	175	139
4 km	(-396,468)	(-1620,-468)	217	289

Table 1-4: Vertical Layer Structure

WRF Layer	Sigma Level	Top (m AGL)	Center (m AGL)	Thickness (m)
44	0.000	20581	20054	1054
43	0.010	19527	18888	1278
42	0.025	18249	17573	1353
41	0.045	16896	16344	1103
40	0.065	15793	15215	1156
39	0.090	14637	14144	987
38	0.115	13650	13136	1029
37	0.145	12621	12168	906
36	0.175	11716	11245	941
35	0.210	10774	10294	962
34	0.250	9813	9379	867
33	0.290	8946	8550	792
32	0.330	8154	7790	729
31	0.370	7425	7128	594
30	0.405	6830	6551	559
29	0.440	6271	6007	528
28	0.475	5743	5492	501
27	0.510	5242	5037	410
26	0.540	4832	4636	393
25	0.570	4439	4250	378
24	0.600	4061	3878	365
23	0.630	3696	3520	352
22	0.660	3344	3173	341
21	0.690	3003	2838	330
20	0.720	2673	2513	320
19	0.750	2353	2224	259
18	0.775	2094	1967	253
17	0.800	1841	1717	247
16	0.825	1593	1472	242
15	0.850	1352	1280	143
14	0.865	1209	1138	141
13	0.880	1068	999	139
12	0.895	929	860	137
11	0.910	792	746	91
10	0.920	701	656	90

WRF Layer	Sigma Level	Top (m AGL)	Center (m AGL)	Thickness (m)
9	0.930	611	566	89
8	0.940	522	477	89
7	0.950	433	389	88
6	0.960	345	301	87
5	0.970	258	214	87
4	0.980	171	128	86
3	0.990	85	60	51
2	0.996	34	26	17
1	0.998	17	8	17
0	1.000	0	0	0

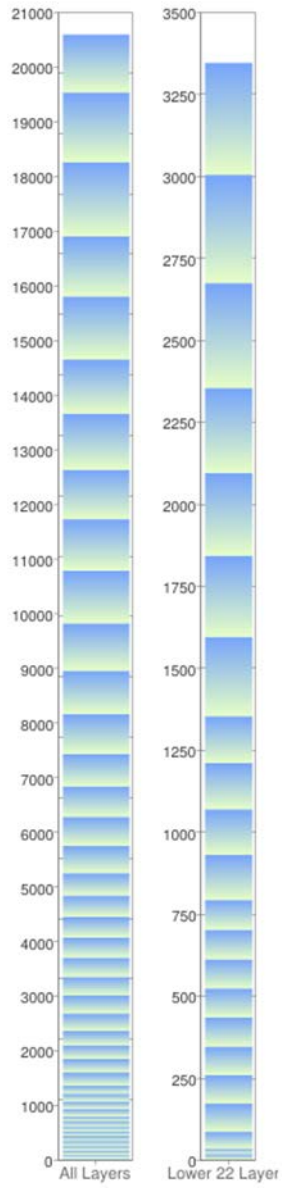

Figure 1-2: WRF Vertical Layer Structure

The WRF vertical layer structure is intended to provide high resolution in the lowest part of the atmosphere where pollutant mixing is critical, as shown in Figure 1-2: *WRF Vertical Layer Structure*. The same WRF vertical layering structure is used for all of the domains.

2. WRF PREPARATION

2.1 WRF Preprocessing System (WPS)

In addition to upgrading to WRF version 3.7.1, the latest WRF modeling involved locating periods of data missing from the GCIP (GEWEX (Global Energy and Water EXperiment) Continental-scale International Project) NCEP (National Centers for Environmental Prediction) Eta archived data that were used to initialize the WRF model and develop model boundary conditions. The preparation of WRF input files involves the execution of different models within the WPS described below.

GEOGRID

- GEOGRID defined the WRF grids on a Lambert-Conformal Projection (see Table 1-2) and allocated the Land Use/Land Cover (LULC) data. New LULC data was included in the WRF v3.7.1 release.

UNGRIB/METGRID

- UNGRIB unpacked the GRIB (Gridded Binary) files with surface and upper level meteorological data to standard pressure levels native to the GCIP NCEP Eta data archive. This archive has the highest temporal resolution (three-hour as well as six-hour) of the archived data available for processing into initial conditions and boundary conditions. These data also extend to 50 millibars (mb), which is higher than other archived data. Both of these features have proven desirable for preparing WRF initial conditions and boundary condition files.
- METGRID re-gridded the unpacked data onto the WRF grids defined in GEOGRID into a NetCDF (Network Common Data Form) format.

MOD_LEVS

- Where data were missing from the GCIP NCEP Eta archive, data extracted from NCEP North American Mesoscale (NAM) model were used. This model is archived on a six-hour interval, compared to the 3-hour interval of the GCIP NCEP Eta. The NAM model extends to 50 mb but has additional pressure levels beyond what is needed to match the GCIP NCEP Eta data. The MOD_LEVS program was run to remove the extra data levels. METGRID was then re-run. Extracting data consistently across matching pressure levels facilitated scripting WRF preprocessing across multiple months.

OBSGRID

- This optional program was used to generate the surface analysis nudging files for the 4 km inner grid. In addition to generating the surface nudging files, new gridded data files consistent with the surface analysis replace the gridded met data for the 4 km grid generated by the METGRID program.

REAL

- The REAL program defined the WRF sigma level vertical structure (Figure 1-2) and mapped the archived data retrieved on pressure levels to the sigma levels defined by the WRF user, consistent with surface land use data and definitions of the upper atmosphere. Base state variables were set to Texas summer values: 1013 hPa sea-level pressure, a reference temperature lapse rate of 45 (K/ln p), and a 304 degrees K sea-level temperature. The REAL program produced the WRF initial condition files, boundary condition files, and WRF FDDA (Four Dimensional Data Assimilation) files, where the four dimensions are three spatial dimensions plus time. WRF Surface FDDA (WRFSFDDA) files were developed during the previous OBSGRID step.

In addition to the analysis nudging files (WRFSFDDA and WRFFDDA) produced during WPS preparation, archived Meteorological Assimilation Data Ingest System (MADIS) boundary layer radar profiler data were processed. The retrieved profiler data were filtered, reorganized, and

reformatted with Python and SAS routines to generate an observational nudging file for the 4 km WRF grid. The profiler locations are shown in Figure 2-1: *Boundary Layer Profilers Active during HGB 2012 Season*. Unlike earlier HGB Attainment Demonstration SIP revision modeling, the 2012 modeling season did not include radar profiler data within the HGB area. However, the NCEP data gridded analyses used by WPS already include all available upper air and surface data, which taken with WRF model system improvements has lessened the dependence on the profiler data for acceptable model performance.

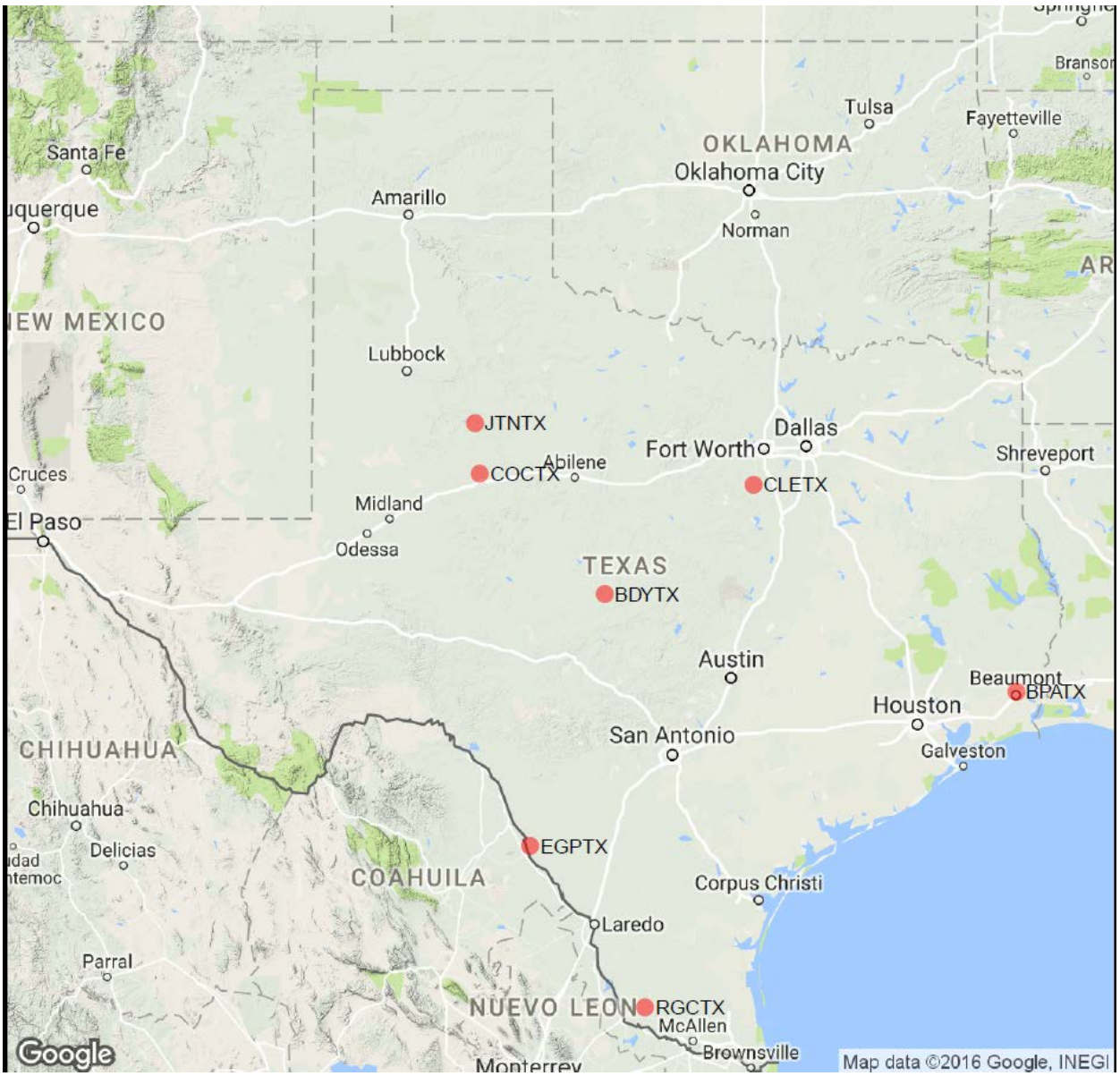

Figure 2-1: Boundary Layer Profilers Active during HGB 2012 Season

Further details about WRF preprocessing can be found at the following URL: http://www2.mmm.ucar.edu/wrf/users/docs/user_guide/users_guide_chap3.htm.

2.2 WPS Quality Assurance

As described above, data from the GCIP NCEP Eta archive were processed with WPS to prepare WRF initial conditions, boundary conditions, and FDDA nudging files. This archive was preferred because surface data were usually available in 3-hour intervals. WPS will interpolate to create 1-hour WRF input files. In many cases, the WPS can interpolate across periods of missing data. Figure 2-2: *Missing upper air data during WPS preprocessing* and Figure 2-3: *Missing surface data during WPS preprocessing* summarize missing data during the 2012 HGB modeling season. Each figure is color coded by number of 3-hour data periods that were missing or had contaminated data during each day in the five month modeling season. As seen in Figure 2-2, most upper data were complete with notable exceptions on May 3, August 21 through 25, and September 1 through 3. Figure 2-3 shows that in addition to the days with extensive missing upper air data, the entire season had at least two 3-hour periods with problematic surface analysis data. Many days during June had particular hours with a temperature of zero degrees Celsius or zero wind speeds across the entire 4 km domain. These days were processed by WPS without crashing. Other days that had complete data that included some corrupted hours caused WPS to crash. Missing data on May 3, May 17, August 21 through 25, and September 1 through 3 were patched with data from the NCEP NAM 12 km model as described above. The "patched" days are shown in Figure 2-4: *WPS patch with NCEP NAM data*. The criteria for patching was missing data greater than or equal to 12 hours (four 3-hour contiguous periods). All other days had problematic hours removed from the ungribbed GCIP NCEP Eta data, and WPS was re-run. The METGRID program internally interpolated across the removed hours. Exceptions to the above procedure are May 3 and September 23, 24, and 27. On May 3, the alternate dataset had missing data and METGRID was used to interpolate across the missing data in the original GCIP NCEP Eta archive. Fortunately, on September 23, 24, and 27, missing data were not contiguous, and therefore METGRID could interpolate across the missing hours.

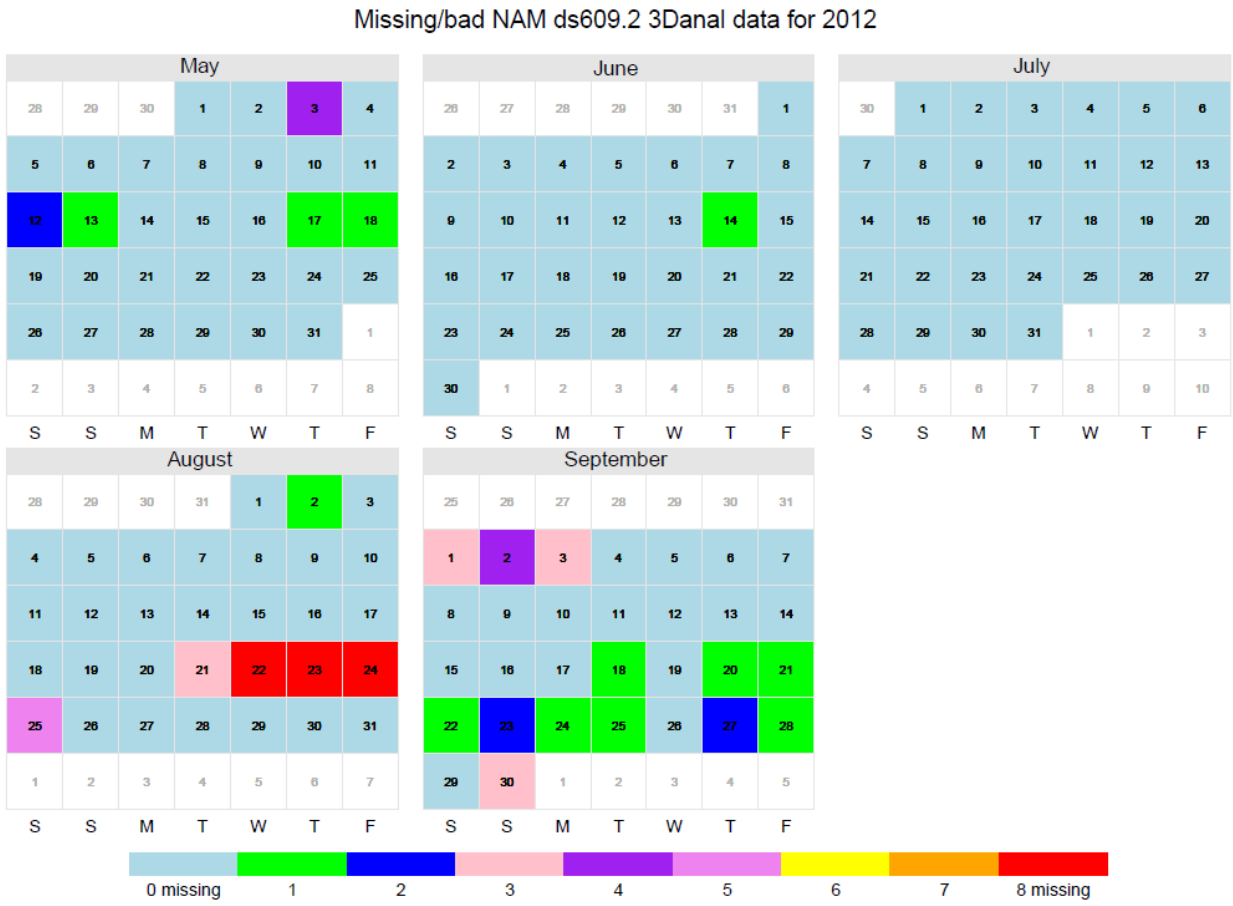

Figure 2-2: Missing Upper Air Data during WPS Preprocessing

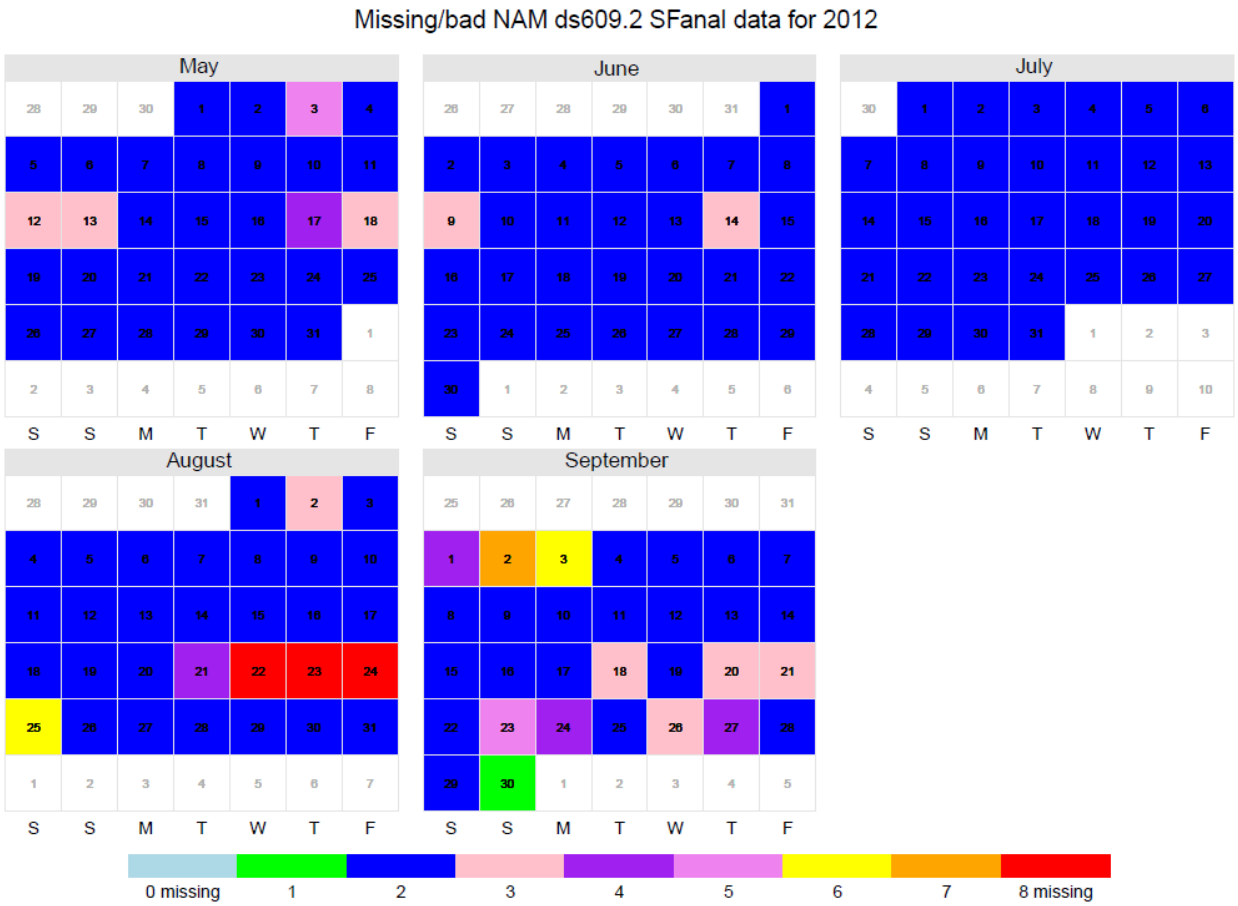

Figure 2-3: Missing Surface Data during WPS Preprocessing

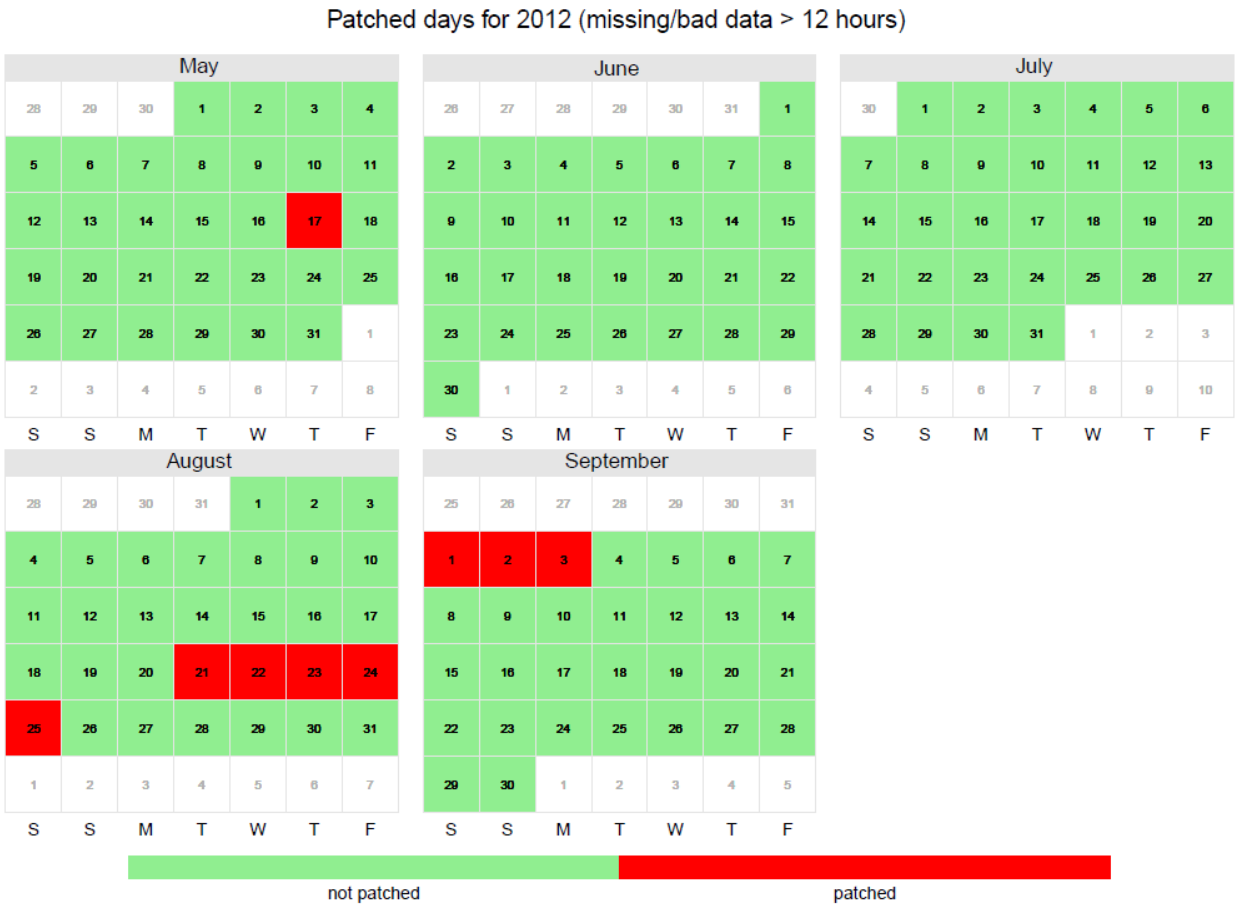

Figure 2-4: WPS Patch with NCEP NAM Data

2.3 WRF Model Configuration

The selection of the final meteorological modeling configuration for the May through September 2012 episode resulted from numerous sensitivity tests and model performance evaluation. The final WRF parameterization schemes and options selected are shown in Table 2-1: *2012 HGB WRF Configuration*. One alternative WRF configuration, part of ongoing work, is to assimilate satellite cloud data into WRF. Basic performance comparisons of configurations are discussed below in Section 4.3: *June 2012 Episode Performance Evaluation of WRF SIP Configuration and Alternate WRF Configuration*.

Table 2-1: 2012 HGB WRF Configuration

Domain	Nudging Type	PBL	Cumulus	Radiation	Land-Surface	Microphysics
36 km and 12 km	3-D Analysis	YSU	Multiscale Kain-Fritsch	RRTM / Dudhia	Pleim-Xiu	WSM5
4 km	3-D, Surface Analysis, & Obs	YSU	Multiscale Kain-Fritsch	RRTM / Dudhia	Pleim-Xiu	WSM6

Note: RRTM = Rapid Radiative Transfer Model

Modeling a five-month episode, like the 2012 HGB modeling platform, benefits from using a land surface model. For periods as short as a month when archived data reflect the default WRF seasonal averages, simple thermal diffusion may provide adequate performance. However, during longer and varied meteorological regimes, modeling soil moisture as well as temperature within a vegetative canopy will provide more realistic surface fluxes. The selected WRF configuration used the Pleim-Xiu (PX) land surface model (LSM) as well as the Multiscale Kain-Fritsch cumulus parameterization. The Kain-Fritsch cumulus scheme modifies the partitioning between parameterized convection and explicit moisture microphysics so that this scheme can be used at all grid resolutions (Bullock, 2015). In the performance overview below, the 2012 HGB WRF configuration will be compared to a WRF configuration using the NOAH (NCEP Oregon State Air Force Hydrological Research Laboratory) LSM. Since the latter WRF configuration will be part of ongoing testing of assimilation of GOES cloud data, the original Kain-Fritsch scheme is still employed.

WRF output was post-processed using the WRFCAMX version 4.3 utility to convert the WRF meteorological fields to the Comprehensive Air Quality Model with Extensions (CAMx) grid and input format (Environ, 2010). The WRFCAMX now generates several alternative vertical diffusivity (Kv) files based upon multiple methodologies for estimating mixing given the same WRF meteorological fields. The WRF Kv option based upon the CMAQ PBL profile was selected.

3. WRF MODEL PERFORMANCE EVALUATION (MPE) TOOLS

3.1 Observations

To evaluate the performance of WRF, comparisons to observed data are made. For surface data, the TCEQ Continuous Air Monitoring Stations (CAMS) are used for comparison. There were over 100 CAMS in the WRF 4 km domain and 25 in the HGB nonattainment area during the 2012 modeling period as shown in Figure 3-1: *CAMS in the 4 km Domain (top) and HGB Area Nonattainment* Area (bottom*)*.

Because of the large number of CAMS monitors in the HGB Region 12, area-wide averaging may inappropriately smooth out smaller scale features. Thus, in addition to the reported Region 12 average accuracy, eight monitors throughout the HGB nonattainment area were selected to represent smaller geographic areas. Also, these monitors have historically captured high ozone events. The performance accuracy at these sites will be reported in summary tables in the monthly discussions below.

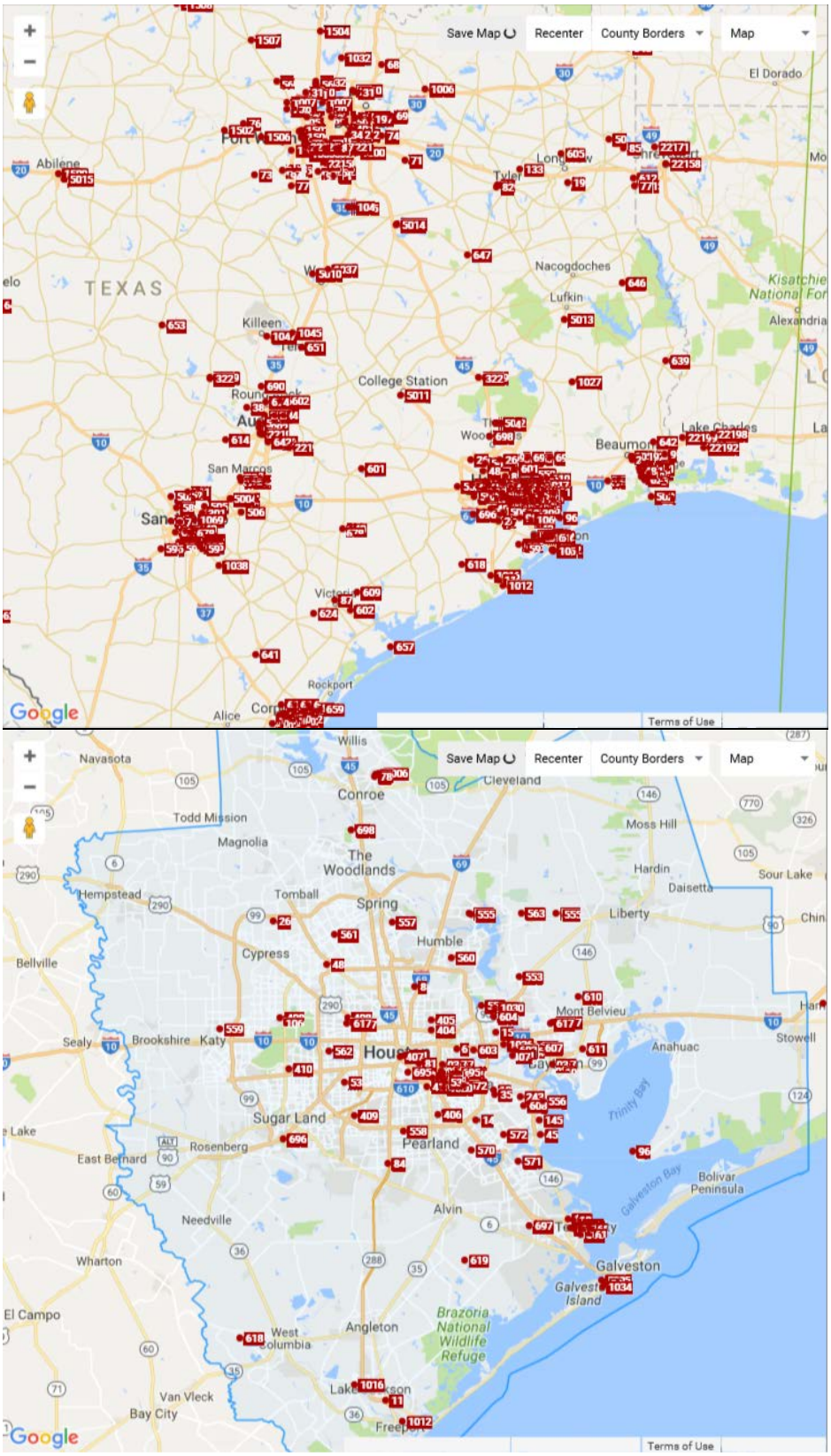

Figure 3-1: CAMS in the 4 km Domain (top) and HGB Area Nonattainment Area (bottom)

3.2 Time Series Panels

Time series panels comparing modeled and observed CAMS surface wind direction, wind speed, and temperature were created to evaluate the model's performance over the entire episode. The observations are hourly averages of individual and grouped monitors (e.g. TCEQ Region 12). An example time series panel in Figure 3-2: *June 2012 HGB* shows hourly wind speed averaged over the CAMS in Region 12. The x-axis of the time series panels is the date and time in Central Standard Time (CST) of the modeling episode. The y-axis represents the range of values of the plotted parameter (e.g. wind speed). The title of the panel indicates the geographic region, meteorological parameter (wind speed, temperature, etc.), and model run name.

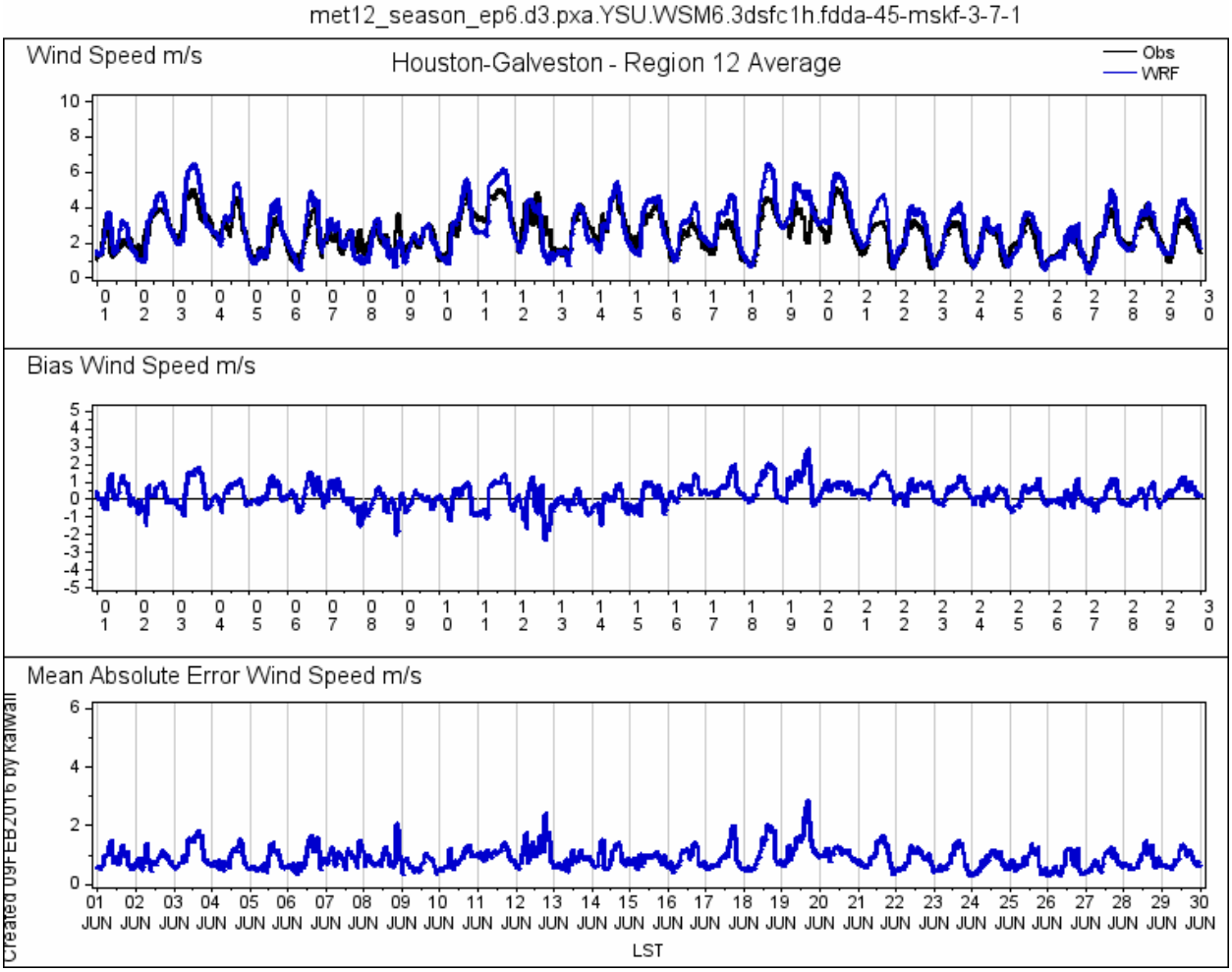

Figure 3-2: June 2012 HGB Wind Speed Time Series

3.3 Scatter Plots

Scatter plots of modeled versus observed concentrations were created to evaluate how well the model performs at monitors (groups of monitors), episode days, and model layers. As with the time series, the model is compared observations averaged across TCEQ Region 12 or individual monitors for every hour (per day or episode). The percent of hours (all, day, or night) where the model is within the accuracy benchmarks (e.g. wind direction less than or equal to 30 degrees or wind speed less than or equal to 2 meters per second (m/s)) is depicted in the upper right of the plot. Tables of these accuracy percentages are also presented.

A linear regression line is fitted to the data and is shown in green. The correlation equation and coefficient of determination R^2 for the regression line is above the plot in green. If the model perfectly fit the data, the regression line would fall on the one-to-one line and the R^2 would be 1.0. The R^2 indicates how well WRF predicts the observations, with higher values indicating better model performance. As the model is an imperfect representation of the real world and the observations have biases, errors, and limitations, a perfect fit is not expected. A perfect fit (or very close to it) may be reason to suspect that WRF is being nudged too strongly. For wind direction, the regression line and R^2 are not calculated since both 0° and 360° symbolize north winds and make those statistics meaningless.

The scatter plot titles convey the same information as those of the time series. The x-axis is the observed data and the y-axis is the modeled. The total number of date-time points (hours) and observations (hour-monitor pairs) that comprise the plot are listed next to the parameter name. Figure 3-3: *June 2012 HGB Wind Speed Scatter Plot* shows an example of the TCEQ Region 12l wind speed performance over the June 2012 episode. Evening wind speeds were replicated well and there was a small positive wind speed bias during the daylight hours. Overall accuracy remains within the standard metric of 2 m/s and the preferred metric of 1 m/s.

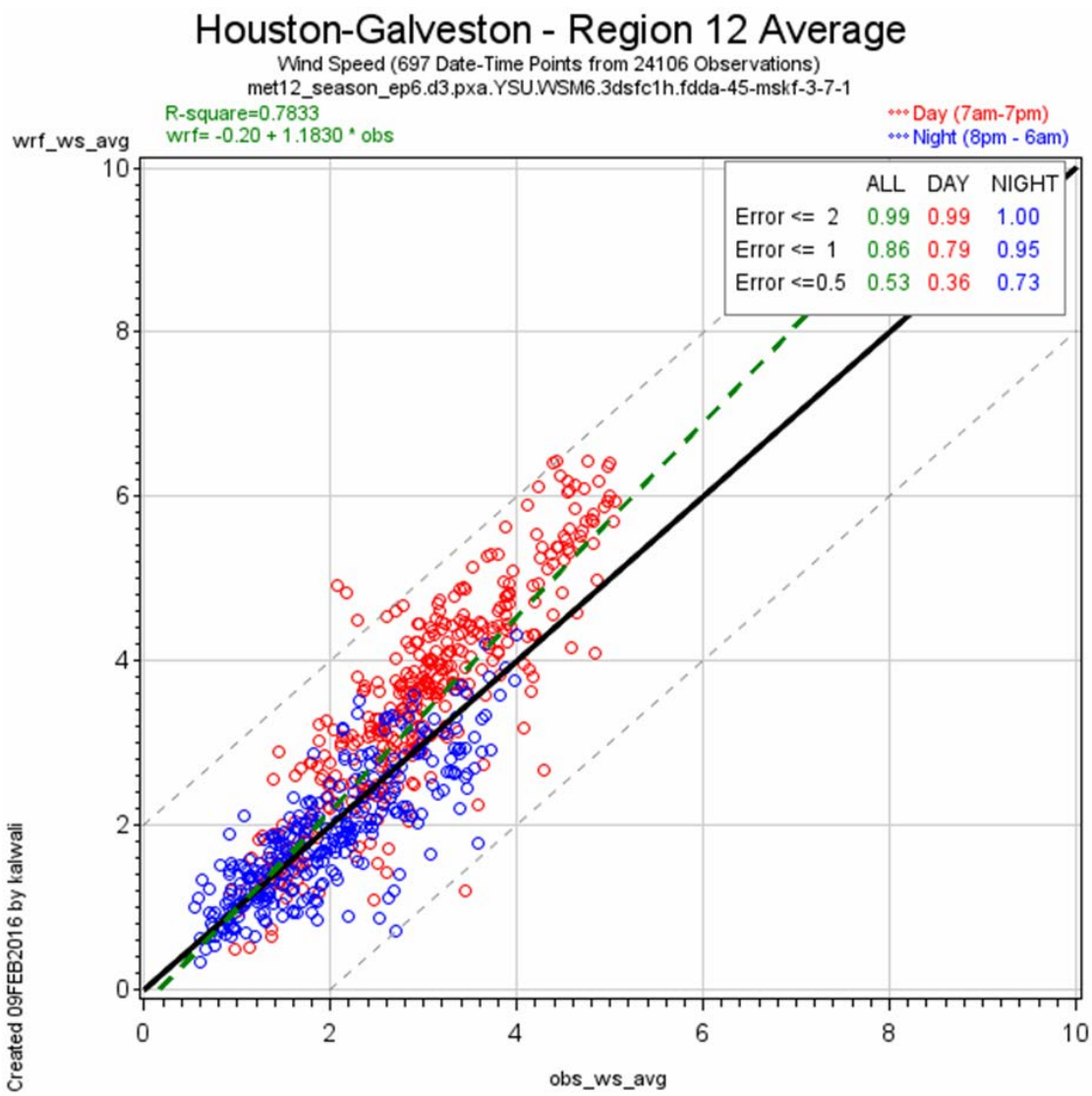

Figure 3-3: June 2012 HGB Wind Speed Scatter Plot

3.4 WRF Cloud Fraction and GOES Cloud Fraction

Early ozone pollution meteorological modeling ignored clouds since episodes were short and selected for clear conditions or occurred during periods of high pressure subsidence associated with ozone production. However, as longer air quality episodes are simulated, the importance of properly capturing cloud coverage increases as longer episodes will include cloudy weather, and subtle cloud differences can strongly affect ozone values.

Cloud images, as captured in the infrared bands of Geostationary Orbiting Environmental Satellite (GOES) data, provide information about the heights of clouds as well as cloud placement. Current GOES data are hourly, and so it is partially useful for timing of clouds as well. Future GOES satellites' data will have a temporal frequency of close to ten minutes and will be increasingly valuable for studying the timing of cloud development and dissipation.

Two WRF fields help evaluate the placement and timing of clouds. One of these is cloud fraction, which has values between zero and one for each model layer. For comparing the GOES data (a

two-dimensional downward looking snapshot) to WRF cloud fraction, the plotted WRF cloud fraction assigned to a grid cell is the maximum cloud fraction in the entire column. An example of the GOES observed cloud fraction is shown in Figure 3-4: *June 26, 2012: 2 pm GOES IR Image*. In the GOES image dark is warm and white is cold; therefore Figure 3-4 shows that much of Texas is cloud-free and warm. The wispy features in the image are low level clouds. Higher level clouds are colder and would appear a brighter white.

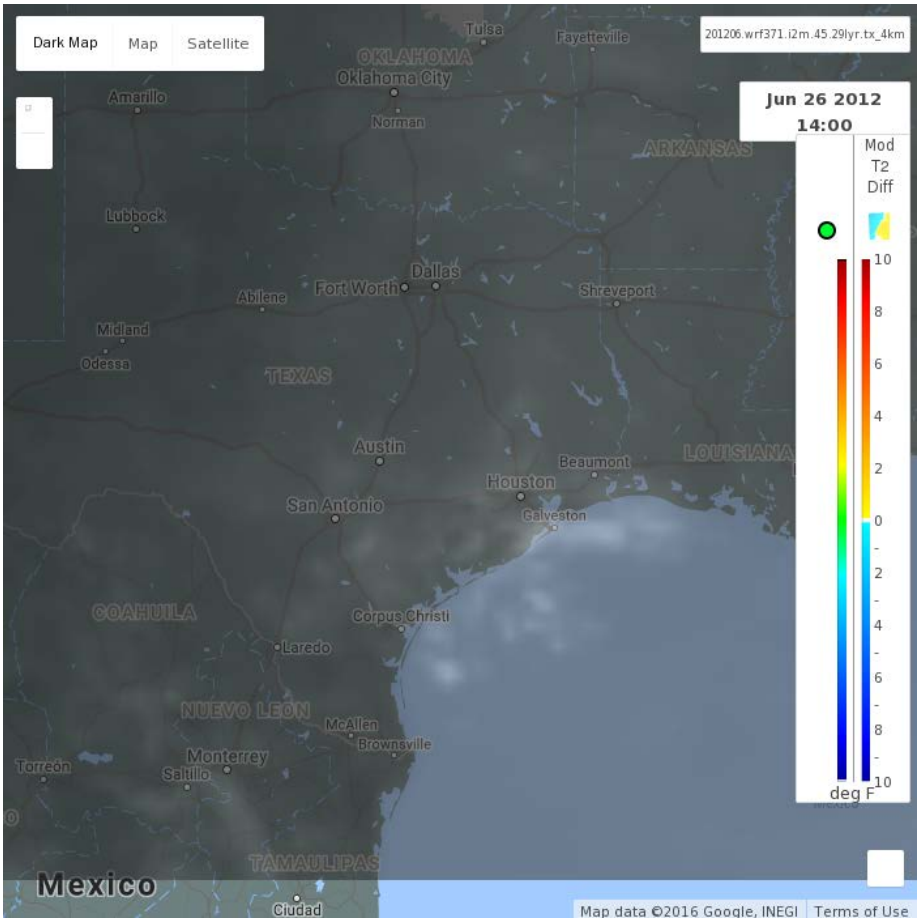

Figure 3-4: June 26, 2012: 2 pm GOES IR Image

Figure 3-4 can be compared to Figure 3-5: *June 26, 2012: 2 pm WRF Maximum Cloud Fraction*. WRF cloud fraction shows high contrast in performance graphics so the predicted extent is easily visualized. However, as mentioned above, the selection of the maximum cloud fraction in each column may be misleading when interpreting WRF clouds, and this graphic will present an "upper bound" on WRF clouds. WRF clouds can also be examined using the WRF shortwave radiative flux described in the next section. This field also presents the extent of WRF clouds with more detailed information about fine scale variability.

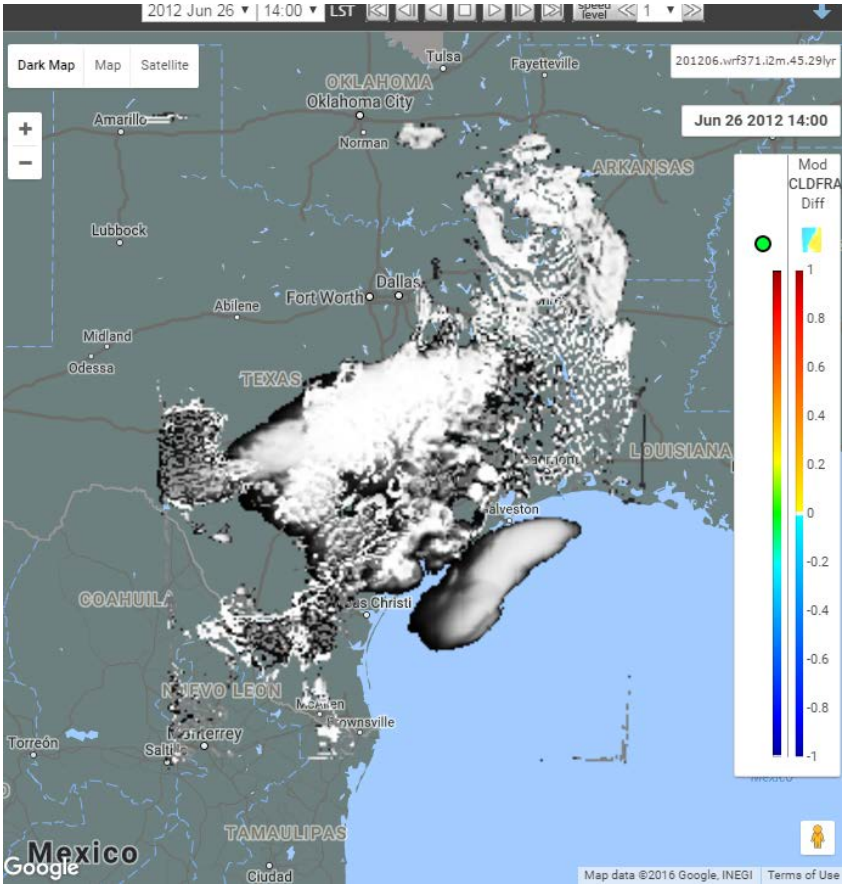

Figure 3-5: June 26, 2012: 2 pm WRF Maximum Cloud Fraction

3.5 WRF Shortwave Radiative Flux and CAMS Shortwave Radiative Flux

A second useful WRF field for evaluating clouds is the shortwave radiative flux (SWDOWN), which is the amount of downward solar radiation reaching the surface of the earth. Evaluation of the shortwave radiative flux complements the GOES IR Image and has the added benefit of being directly comparable to surface solar radiation data.

Figure 3-6: *June 26, 2012: 2 pm WRF Shortwave Radiative Flux Performance* compares the gridded WRF SWDOWN field to CAMS locations collecting solar radiation data. The red color indicates that much of central and west Texas is cloud free at 2 pm CST. However, along the coast there is quite a bit of variability in the shortwave radiative flux. Some regions have large amounts of solar radiation near cloudy areas, which obscure most of shortwave radiation. The CAMS data (identified by the colored dots) also reflect strong variability over a small spatial scale. Modeling clouds on fine spatial and temporal scales is challenging, even when the broad features may appear reasonable.

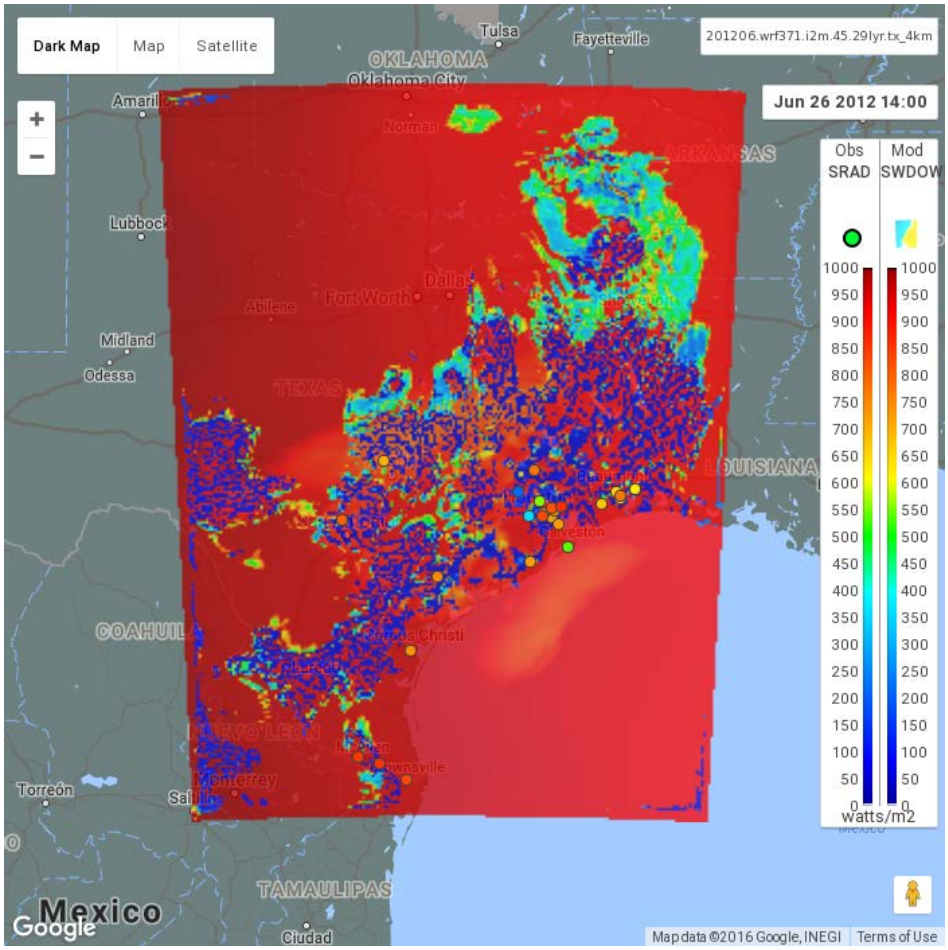

Figure 3-6: June 26, 2012: 2 pm WRF Shortwave Radiative Flux Performance

4. WRF MODELING PERFORMANCE

The following sections describe the performance of the final WRF modeling configuration for the selected days during the HGB 2012 modeling episode. Due to the large number of days, the performance evaluation will focus on the days when high ozone and notable meteorological phenomena occurred. The highest eight-hour ozone day for the 2012 HGB modeling season was June 26 with a maximum eight-hour value of 137.5 ppb, and eight sites had eight-hour values of 100 ppb or higher. In total, four of the top five observed eight-hour ozone days occurred in June. May 2012 had three of the highest eight-hour ozone days, following by August with two (including the fourth highest eight-hour value for the season). September rounded out the top ten with an 87.8 ppb on September 20. Wind field performance continues to be the most important meteorological variable for photochemical modeling input, but temperatures and cloud cover are important indicators of whether mixing throughout the planetary boundary layer (PBL) is captured appropriately.

4.1 May 2012 Episode Performance Evaluation

Figure 4-1: *May 2012 HGB Wind Direction Time Series* captures important features on the high ozone days of May 14, 17, and 21. During May 14 and 17, there is a clockwise veering from northerly flow to southerly flow. May 21 has a flow reversal as the sea breeze becomes established. Both of these features are associated with high ozone days as detailed in Appendix

D: *Conceptual Model for the HGB Attainment Demonstration SIP Revision for the 2008 Eight-Hour Ozone Standard*. The monitors observing the highest ozone also reflect these features. Veering clockwise surface winds frequently place high ozone on the south or southwest side of Houston. On May 14, the peak measured eight-hour ozone concentration was at UH Sugarland, and on the May 17 it was at Manvel Croix Park. The veering winds in Figure 4-2: *May 14, 2012 HGB Wind Direction Scatter Plot* show the May 14 daytime winds distributed between north/northeast and south. On May 21, the highest eight-hour ozone concentrations were at Seabrook, Texas City, and the UH Coastal Center. Although a "classic" flow reversal would show nighttime winds clustered from the northwest and a daytime sea breeze from the southeast, Figure 4-3: *May 21, 2012 HGB Wind Direction Scatter Plot* shows that morning winds were from the northwest and the afternoon sea breeze crossed the coast from the south/southwest.

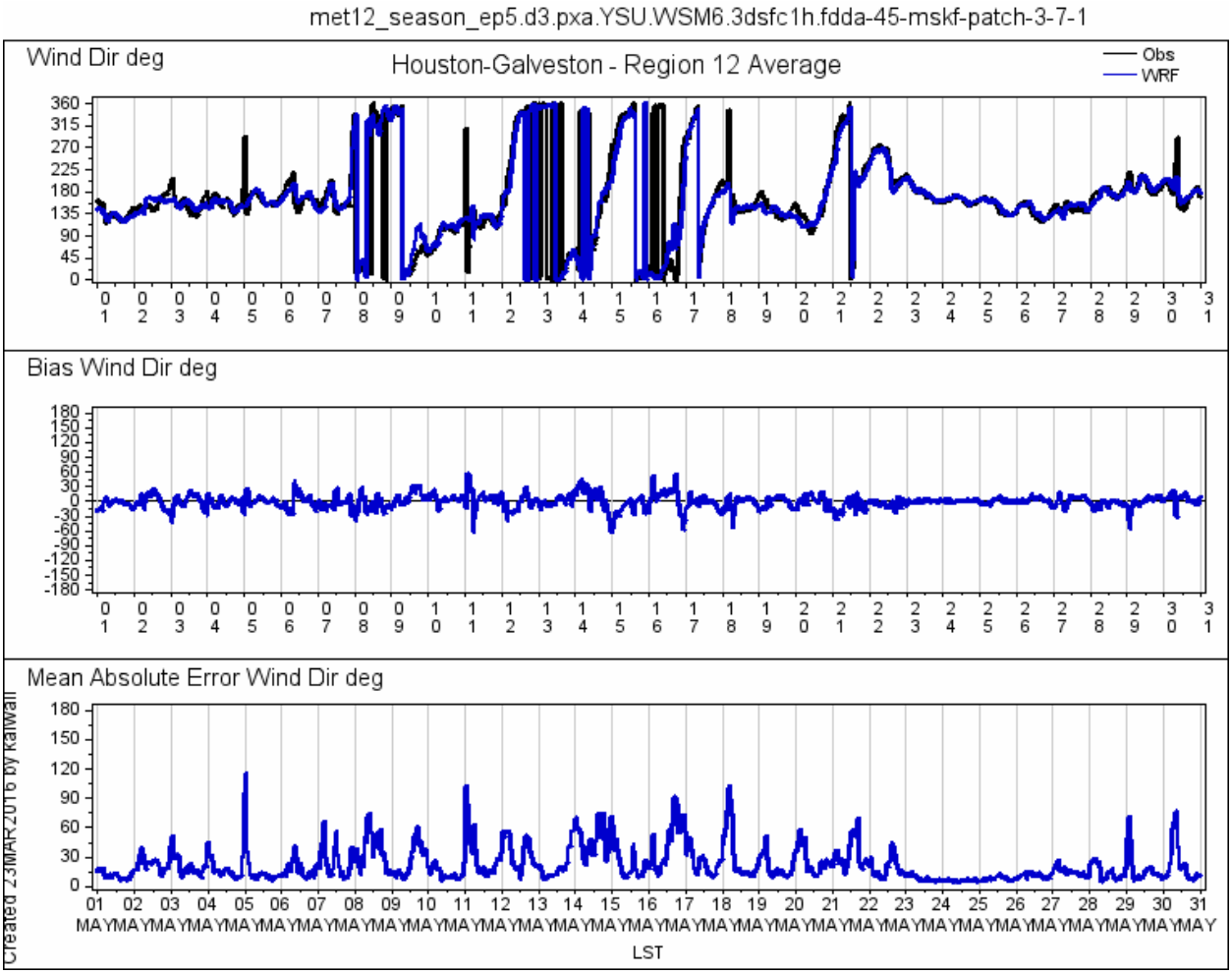

Figure 4-1: May 2012 HGB Wind Direction Time Series

The model showed no appreciable bias in wind direction during May; however, the model missed wind direction shifts close to midnight on May 5, 11, and 18 (see Figure 4-1). Winds speeds on May 5 and 18 were approximately 1 m/s, a difficult speed to replicate. Wind speed performance through the entire month was very good with minimal bias and errors (see Figure 4-4: *May 2012 HGB Wind Speed Time Series*). The role of very light winds on May 21 is depicted in Figure 4-5: *May 21, 2012 HGB Wind Speed Scatter Plot*.

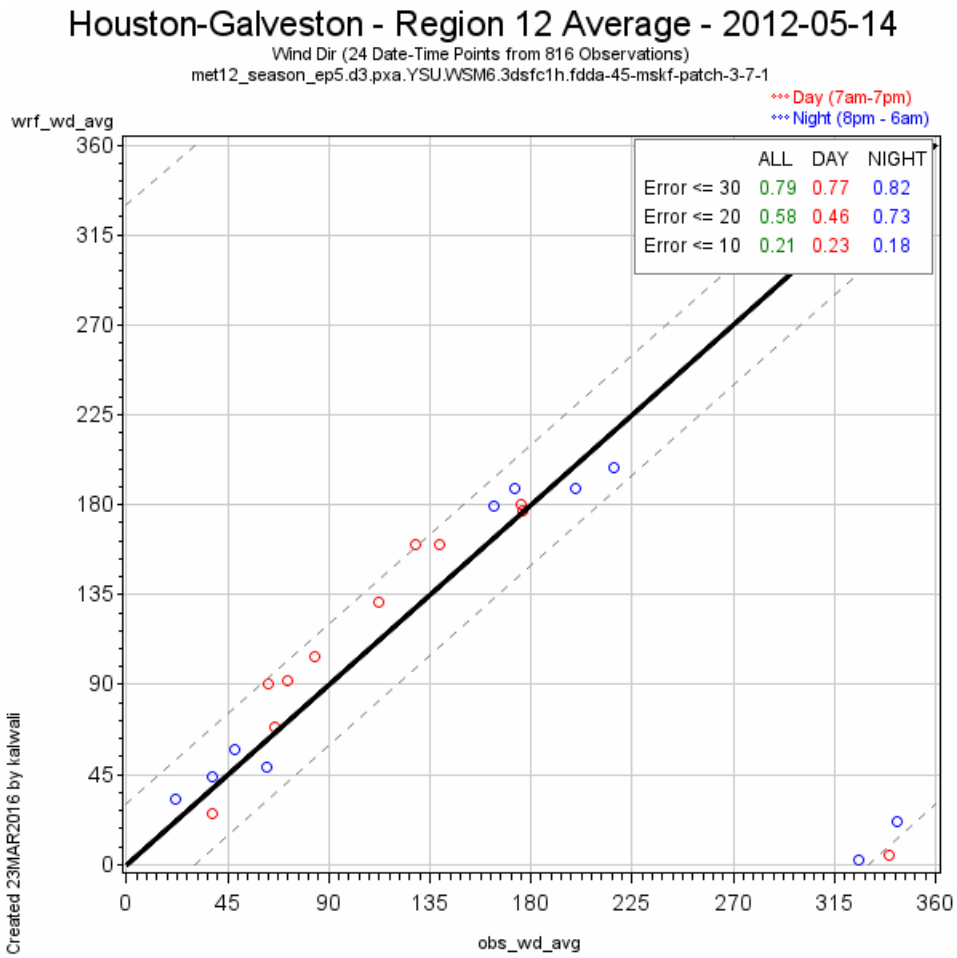

Figure 4-2: May 14, 2012 HGB Wind Direction Scatter Plot

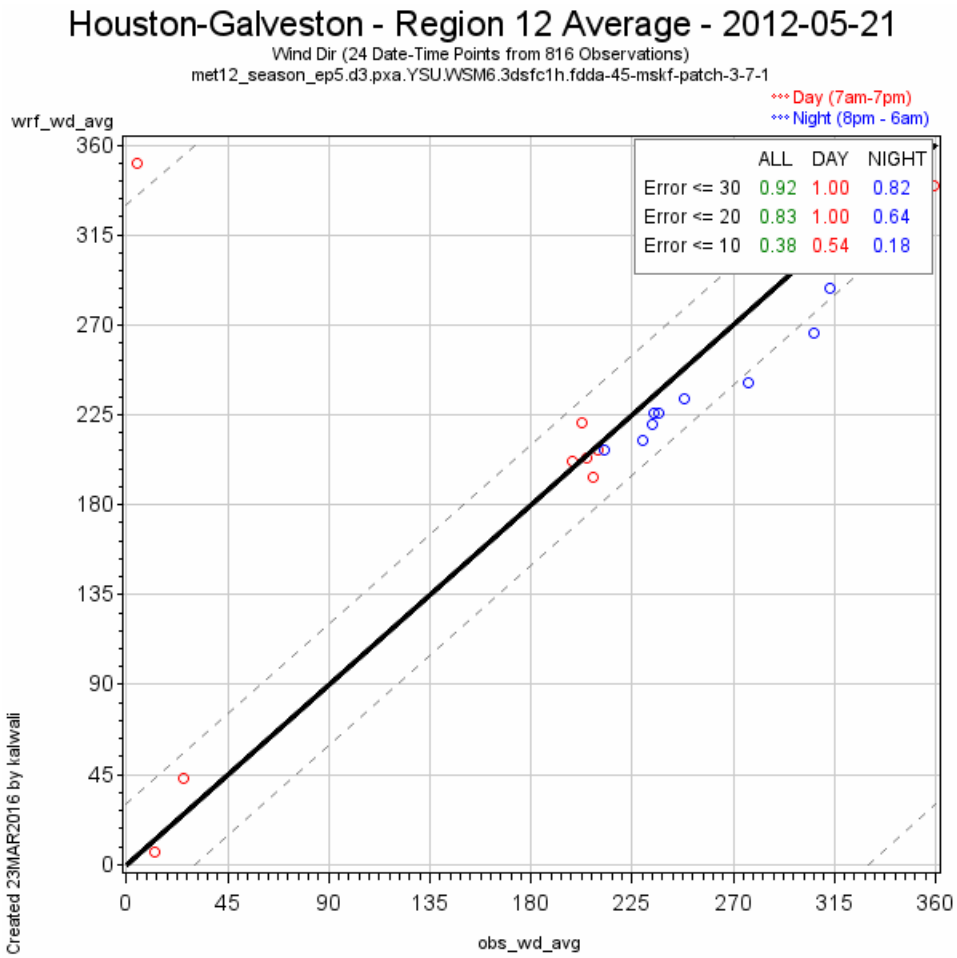

Figure 4-3: May 21, 2012 HGB Wind Direction Scatter Plot

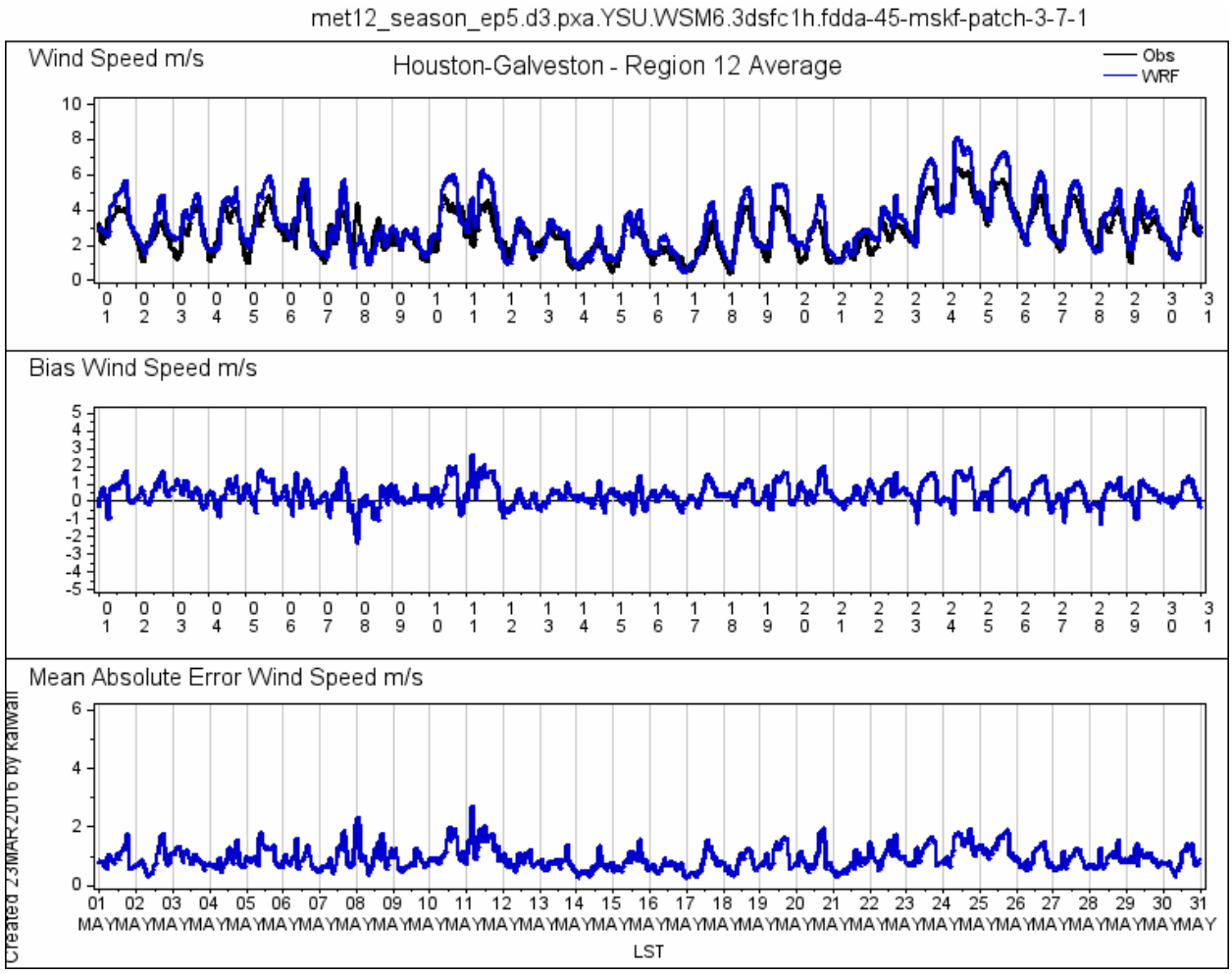

Figure 4-4: May 2012 HGB Wind Speed Time Series

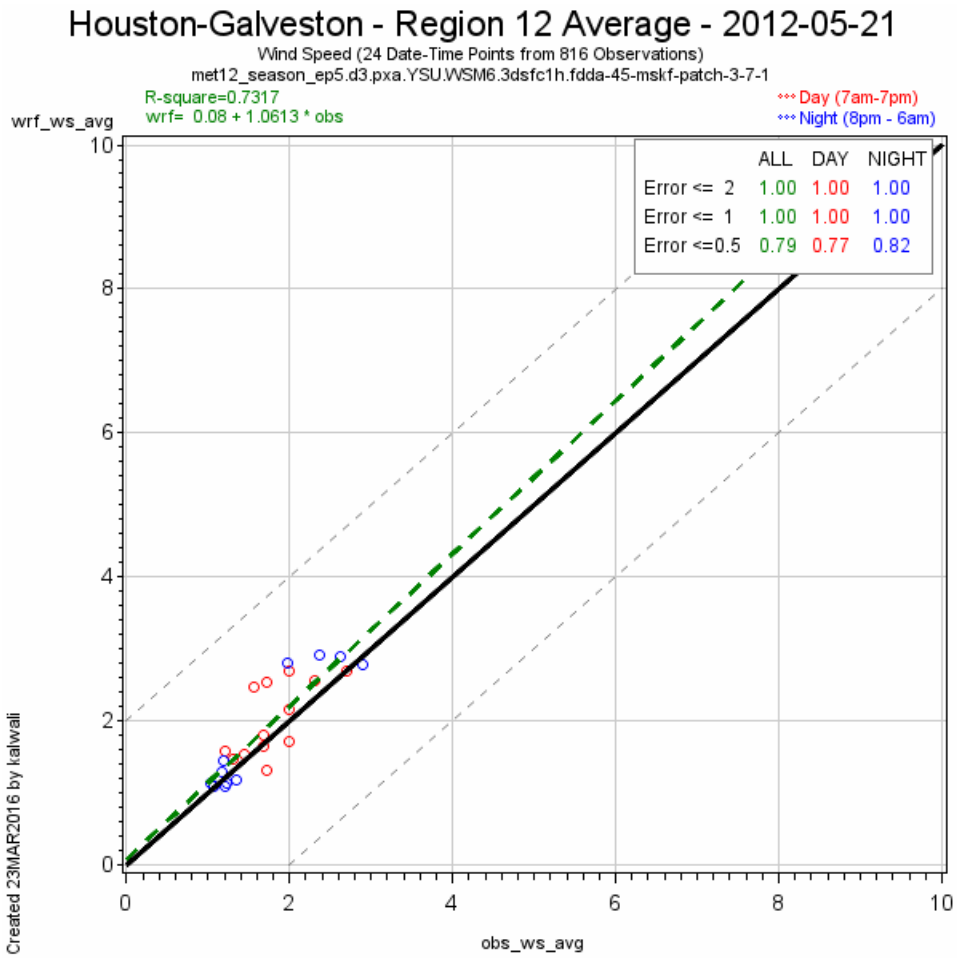

Figure 4-5: May 21, 2012 HGB Wind Speed Scatter Plot

Figure 4-6: *May 2012 HGB Temperature Time Series* shows regional temperature performance that has a weak diurnal bias. The daily errors are often close to 1 degree Kelvin, and with the exception of May 15, tend to stay below 2 degrees Kelvin.

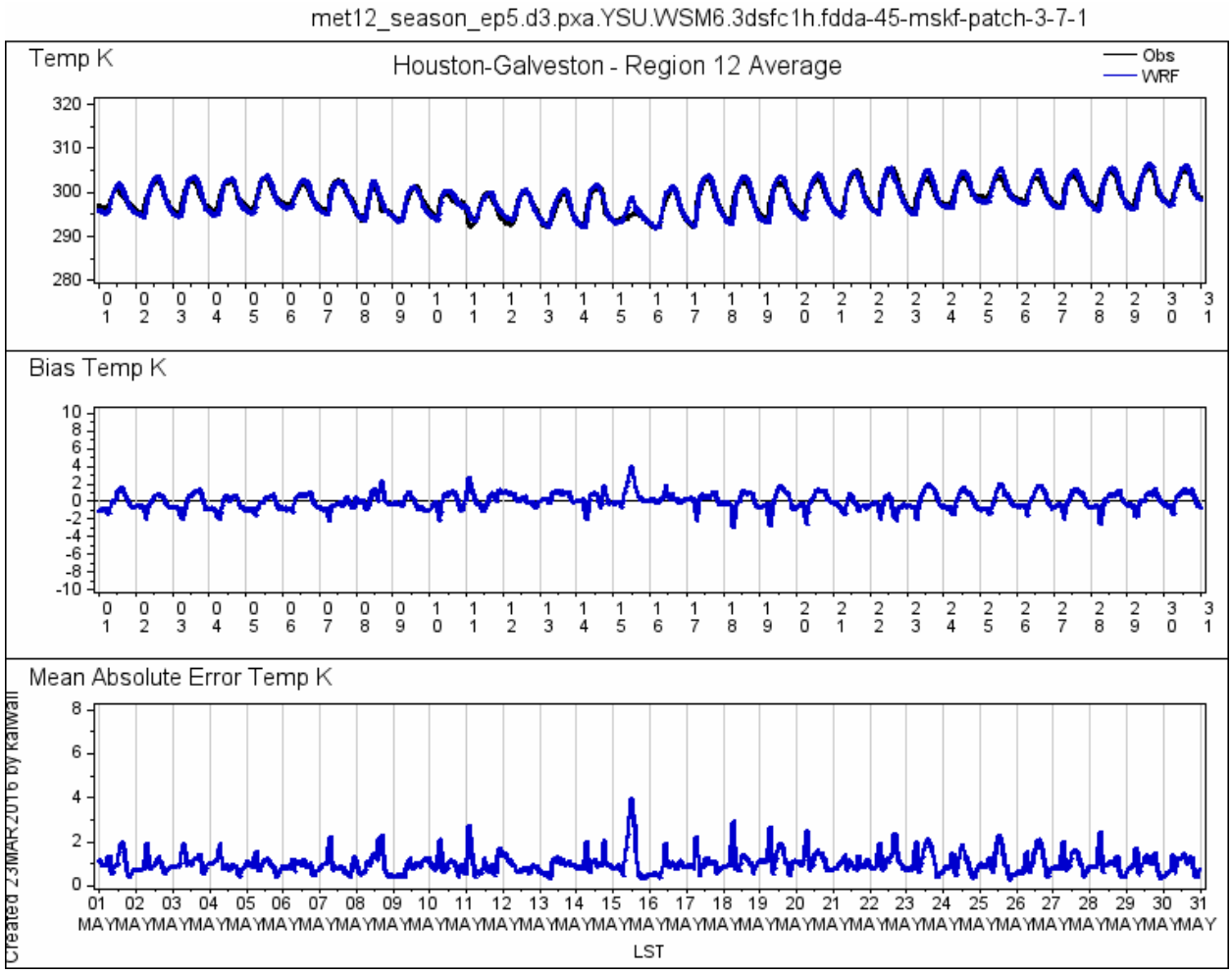

Figure 4-6: May 2012 HGB Temperature Time Series

WRF cloud prediction is generally much improved over earlier models. However, WRF overestimated some clouds in May 2012, which might affect temperature, photolysis, and other parts of the photochemical modeling process. Both Figure 4-7: *May 14, 2012: 2 pm WRF Shortwave Radiative Flux Performance* and Figure 4-8: *May 21, 2012: 2 pm WRF Shortwave Radiative Flux Performance* indicate that downward shortwave radiation was modeled with high spatial variability. There is high spatial variability in the observed data as well. The high spatial variability indicates shortwave radiation changed significantly over short distances, most likely due to small clouds. This reflects the challenge of verifying modeled cloud performance.

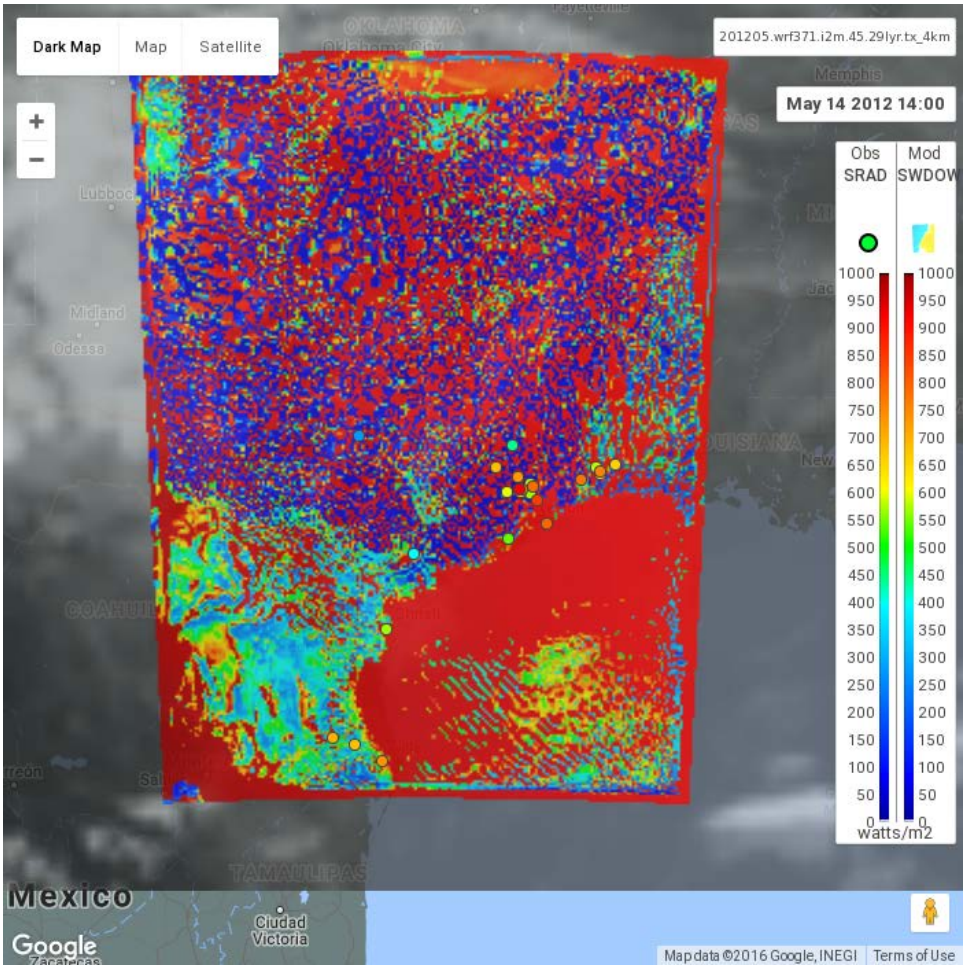

Figure 4-7: May 14, 2012: 2 pm WRF Shortwave Radiative Flux Performance

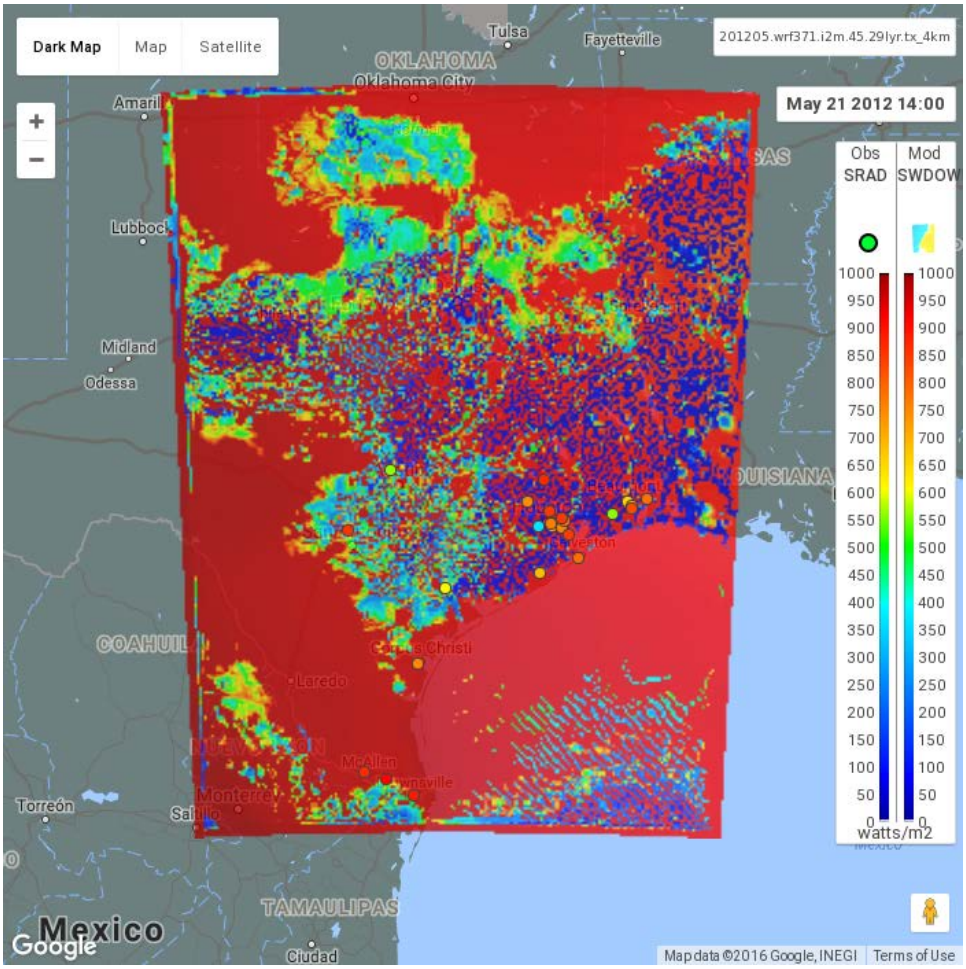

Figure 4-8: May 21, 2012: 2 pm WRF Shortwave Radiative Flux Performance

May 2012 meteorological modeling performance is summarized in Table 4-1: *May 2012 HGB Meteorological Modeling Percent Accuracy*. The first performance benchmark for each parameter has been consistently used to characterize desirable performance (Emery, 2001). The tighter bounds for wind direction, wind speed, and temperature are also included. Given the general complex meteorology along the Texas coast, these statistics are considered reasonably robust.

Table 4-1: May 2012 HGB Meteorological Modeling Percent Accuracy

HGB Area	Wind Direction (°) Error ≤ 30 / 20 / 10	Wind Speed (m/s) Error ≤ 2 / 1 / 0.5	Temperature (°C) Error ≤ 2 / 1 / 0.5
Region 12 Average	91 / 83 / 57	99 /79 / 54	98 / 76 / 40
Manvel Croix	77 / 64 / 42	95 / 69 / 37	89 /54 / 14
Deer Park	81 / 67 /36	96 / 67 / 39	90 / 58/ 33
Clinton Drive	60 / 39 / 18	91 / 58 / 35	88 / 48 / 22
Channelview	72 / 58 / 34	92 / 73 /43	78 / 40 / 19
Aldine	75 / 62 / 35	98 / 76 / 48	95 / 67 / 39
Bayland Park	81 / 72 / 49	97 / 82 / 52	91 / 63 / 36

HGB Area	Wind Direction (°) Error ≤ 30 / 20 / 10	Wind Speed (m/s) Error ≤ 2 / 1 / 0.5	Temperature (°C) Error ≤ 2 / 1 / 0.5
Northwest Harris Co.	73 / 62 / 38	93 / 65 / 35	94 / 63 / 39
Conroe	73 / 62 / 40	97 / 80 / 51	92 / 65 / 39

4.2 June 2012 Episode Performance Evaluation

Figure 4-9: *June 2012 HGB Wind Direction Time Series* shows that June had minimal wind direction bias throughout the month, including high ozone days. High errors on some days (June 8, 18, and 23) near midnight were associated with exceptionally light winds. The two highest ozone days of June 1 and 26 display clockwise veering of surface winds between northerly to southerly and northwesterly to southwesterly flows respectively (see Figure 4-10: *June 1, 2012 HGB Wind Direction Scatter Plot* and Figure 4-11: *June 26, 2012 HGB Wind Direction Scatter Plot*).

On the high ozone days of June 1, 5, 7, 9, 25 through 27, the HGB area had light wind speeds and model performance was very good as shown in Figure 4-12: *June 2012 HGB Wind Speed Time Series*. The lack of high ozone on June 22 and 23 may be partially attributed to slightly higher daytime wind speeds, but also arrival of stagnation later in the afternoon than on the highest day of June 26.

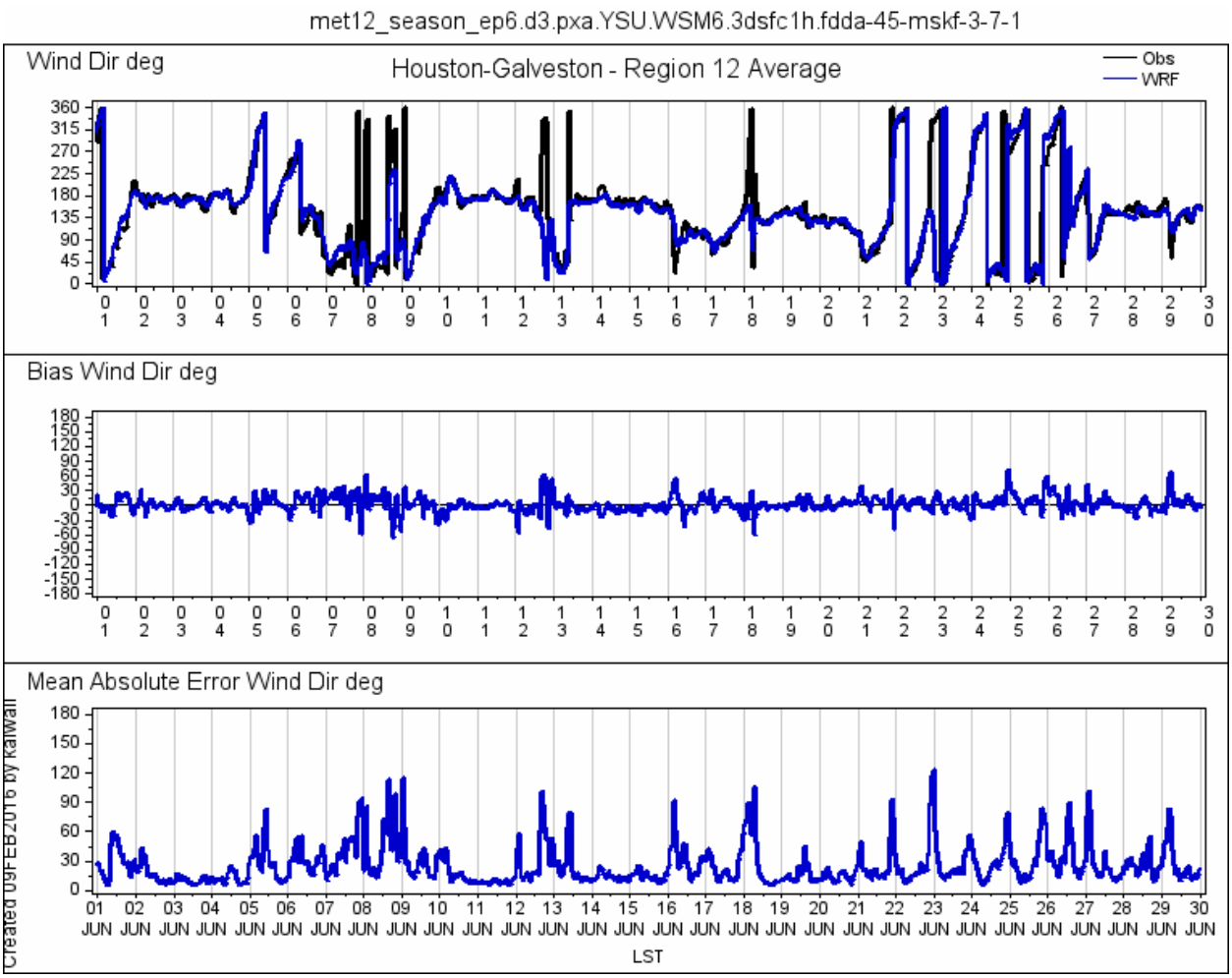

Figure 4-9: June 2012 HGB Wind Direction Time Series

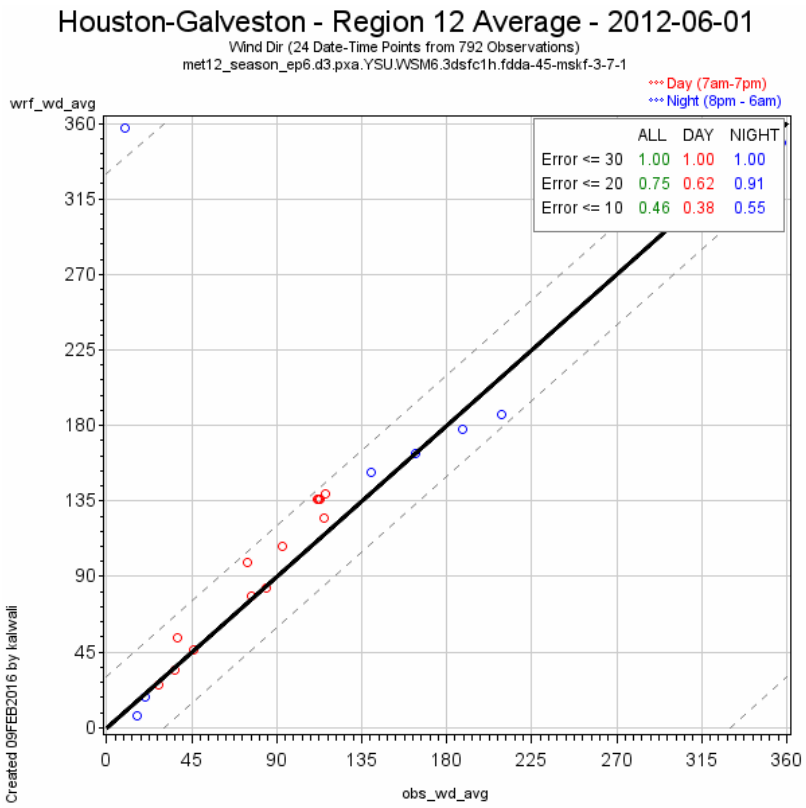

Figure 4-10: June 1, 2012 HGB Wind Direction Scatter Plot

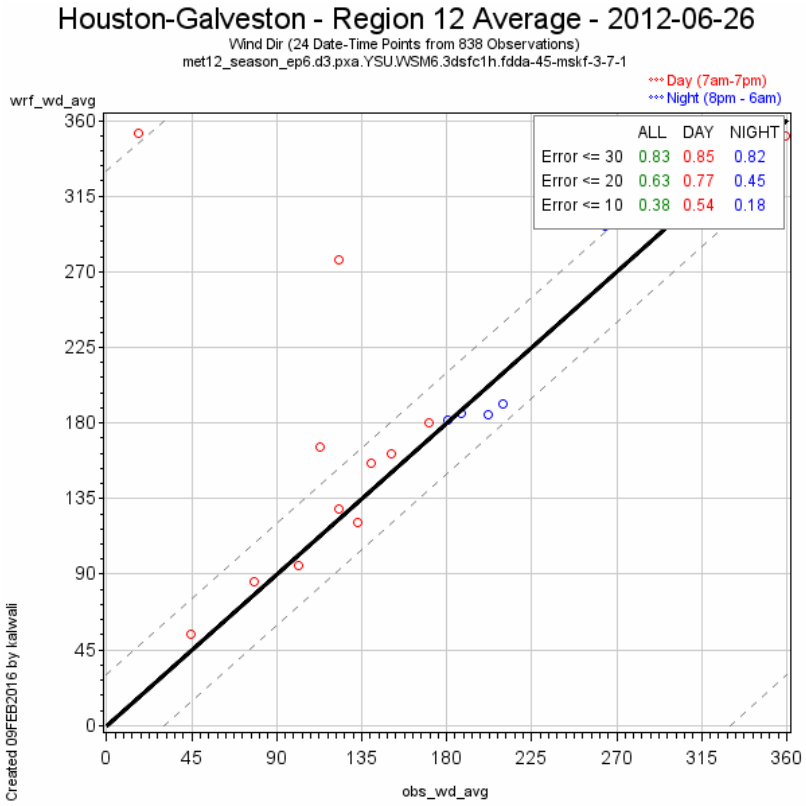

Figure 4-11: June 26, 2012 HGB Wind Direction Scatter Plot

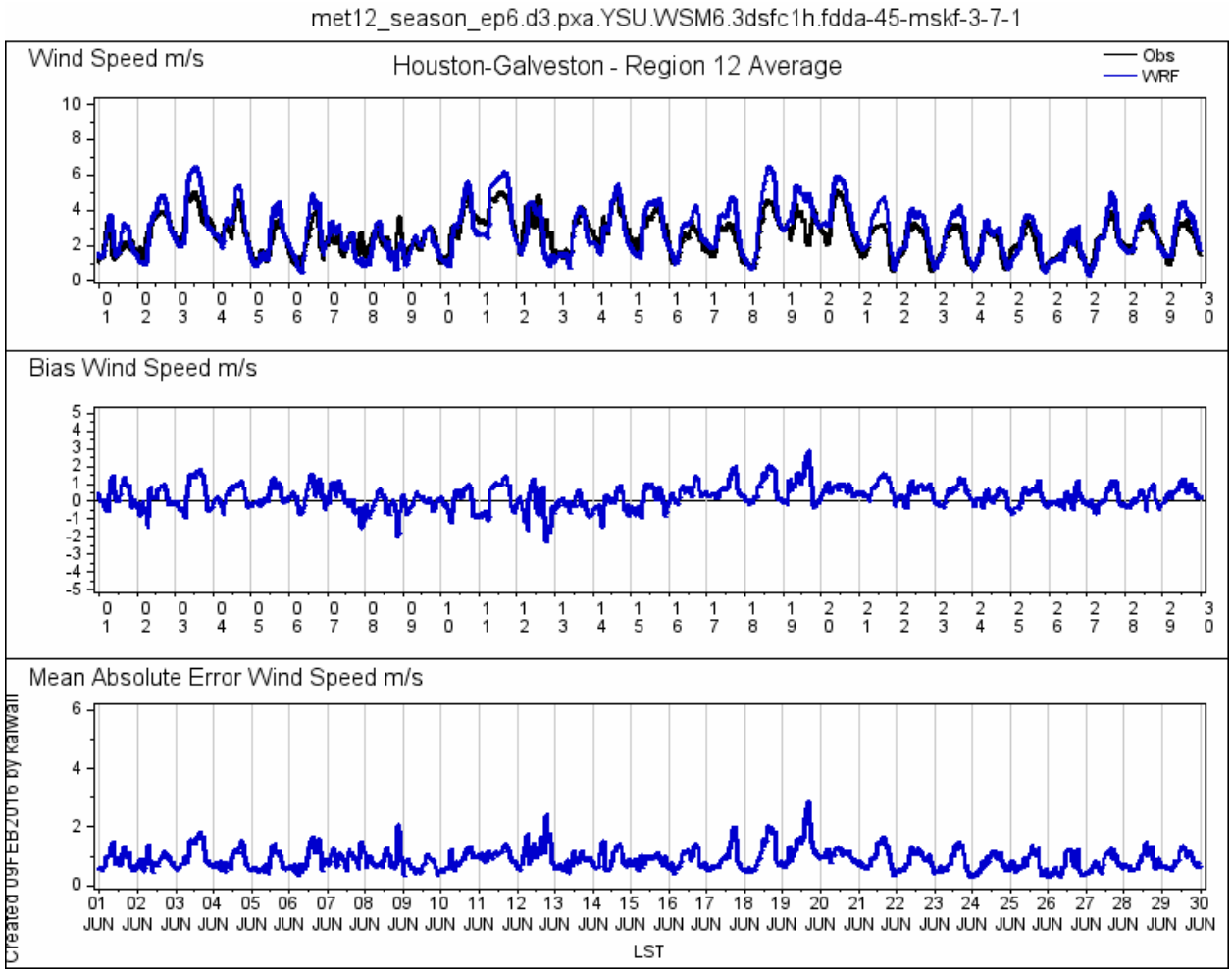

Figure 4-12: June 2012 HGB Wind Speed Time Series

The temperature performance for June presented in Figure 4-13: *June 2012 HGB Temperature Time Series* shows very little diurnal bias. Temperatures were the higher than average temperatures at the end of June, including June 26, which peaked near 100 degrees Fahrenheit.

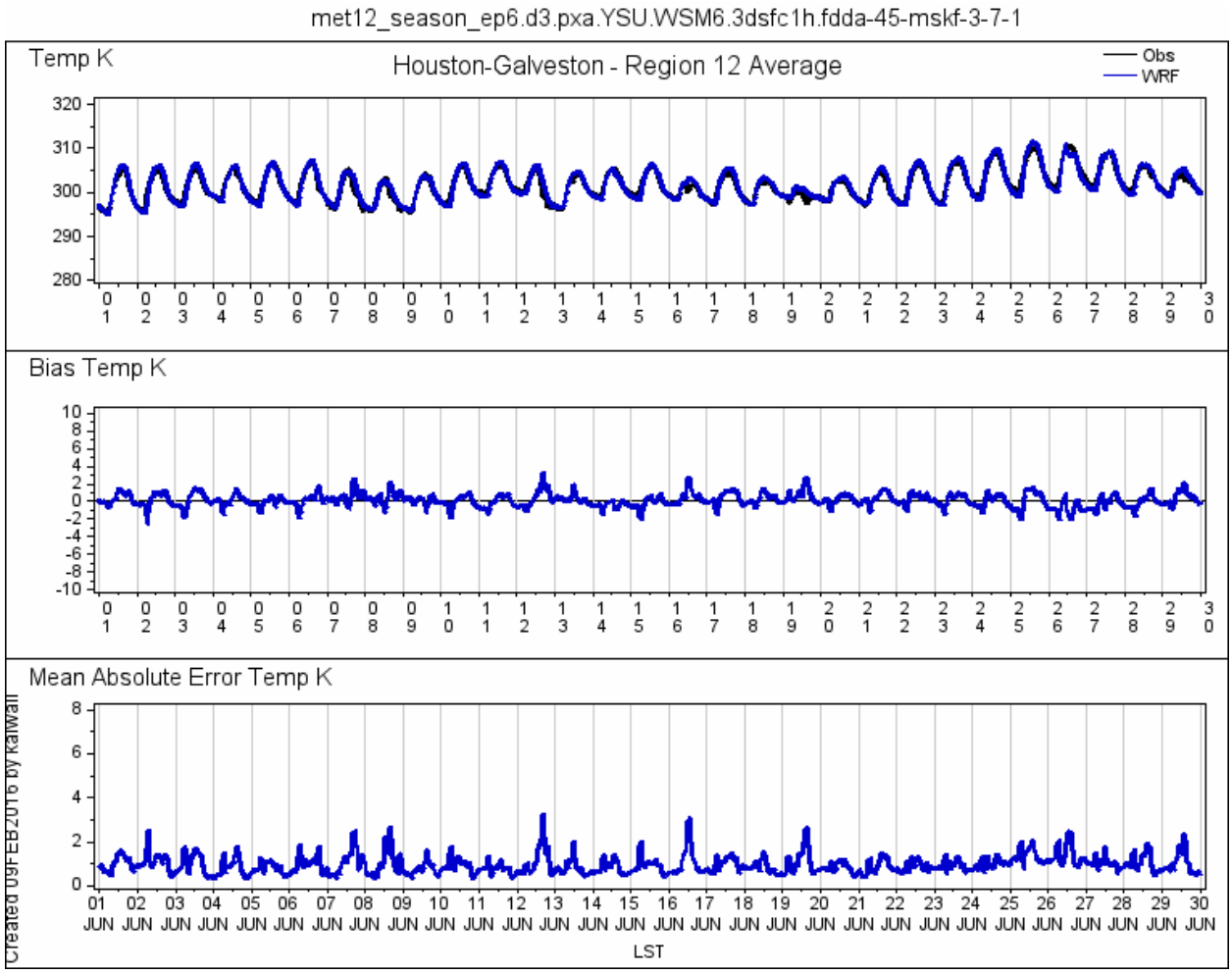

Figure 4-13: June 2012 HGB Temperature Time Series

The relatively clear skies of June 1 were well replicated in WRF, as shown in Figure 4-14: *June 1, 2012 12 pm WRF Shortwave Radiative Flux Performance*. On June 26, WRF-predicted shortwave radiation may be lower than Houston-area observations as displayed in Figure 4-15: *June 26, 2012 12 pm WRF Shortwave Radiative Flux Performance* and Figure 4-16: *June 26, 2012 3 pm WRF Shortwave Radiative Flux Performance*. This may contribute to under-prediction of hourly ozone values at some monitors. The same situation is seen on June 27 in Figure 4-17: *June 27, 2012 2pm WRF Shortwave Radiative Flux Performance*.

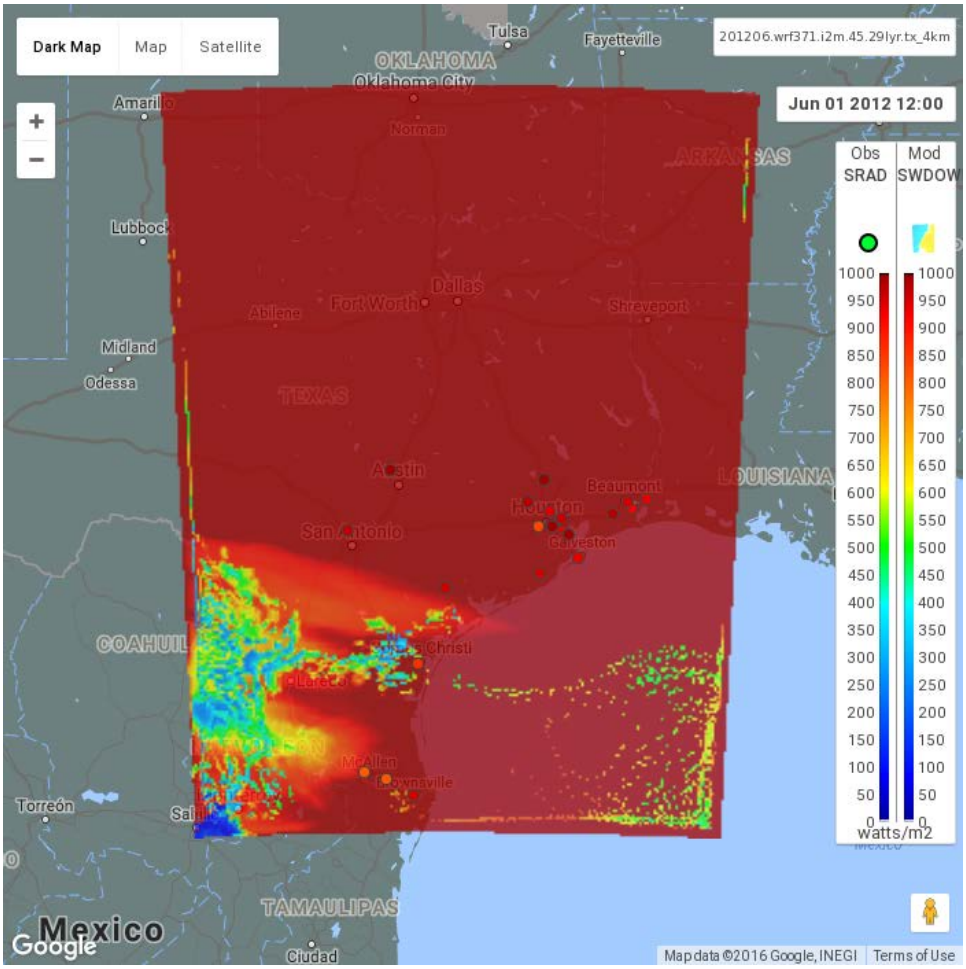

Figure 4-14: June 1, 2012 12 pm WRF Shortwave Radiative Flux Performance

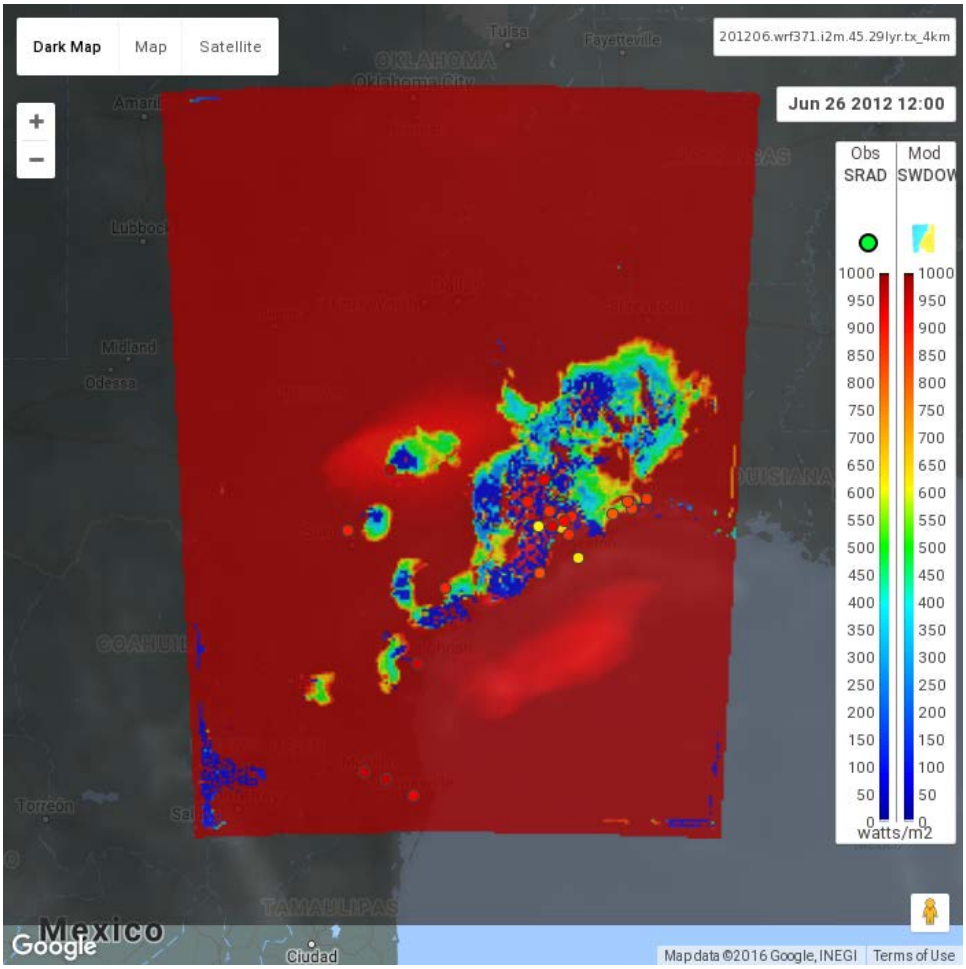

Figure 4-15: June 26, 2012 12 pm WRF Shortwave Radiative Flux Performance

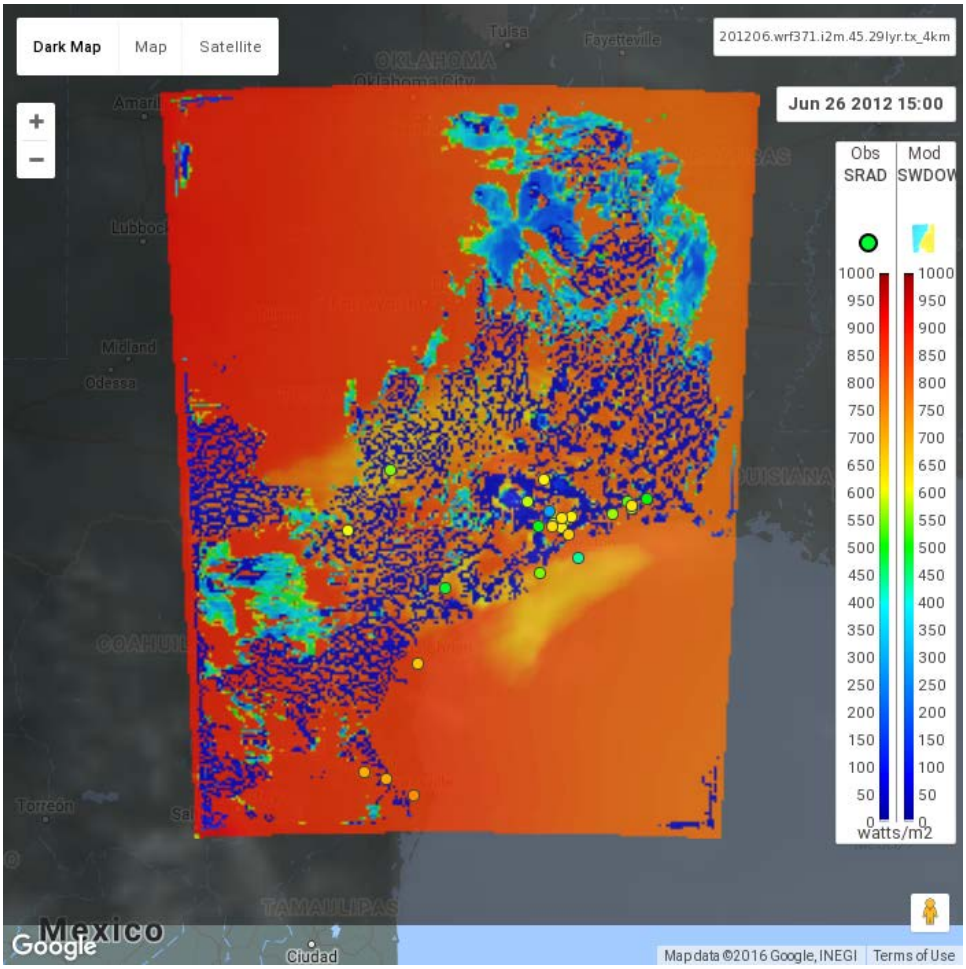

Figure 4-16: June 26, 2012 3 pm WRF Shortwave Radiative Flux Performance

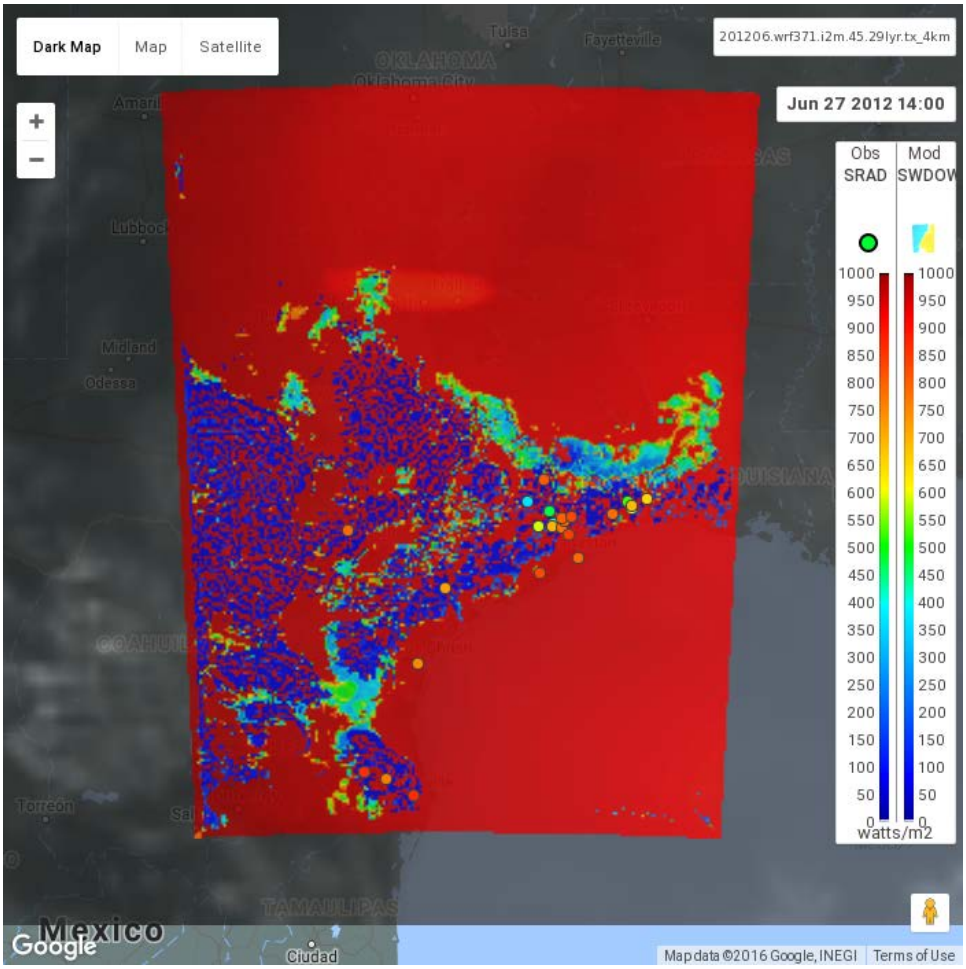

Figure 4-17: June 27, 2012 2pm WRF Shortwave Radiative Flux Performance

Monthly performance accuracy metrics are presented in Table 4-2: *June 2012 HGB Meteorological Modeling Percent Accuracy*.

Table 4-2: June 2012 HGB Meteorological Modeling Percent Accuracy

HGB Area	Wind Direction (°) Error ≤ 30 / 20 / 10	Wind Speed (m/s) Error ≤ 2 / 1 / 0.5	Temperature (°C) Error ≤ 2 / 1 / 0.5
Region 12 Average	90 / 80 / 58	99 /86 / 53	98 / 81 / 53
Manvel Croix	73 / 61 / 39	95 / 76 / 48	89 /60 / 36
Deer Park	76 / 64 /40	94 / 67 / 38	90 / 57/ 27
Clinton Drive	60 / 36 / 14	88 / 59 / 35	91 / 53 / 26
Channelview	70 / 53 / 28	93 / 70 /45	89 / 51 / 25
Aldine	69 / 54 / 31	97 / 79 / 51	95 / 76 / 46
Bayland Park	75 / 66 / 42	96 / 80 / 52	92 / 63 / 38
Northwest Harris Co.	69 / 54 / 31	94 / 72 / 43	92 / 67 / 39
Conroe	71 / 55 / 32	94 / 75 / 48	91 / 65 / 38

4.3 June 2012 Episode Performance Evaluation of WRF SIP Configuration and Alternate WRF Configuration

With longer modeling episode seasons and lower ozone standards, cloud placement is increasingly an important meteorological contributor to air quality modeling performance. The assimilation of satellite-based cloud data is an area of development and research (Biazar et. al., 2015). Although preliminary, an alternate WRF configuration with GOES cloud assimilation was developed. This alternative WRF configuration used the NOAH LSM instead of the PX scheme, the Thompson microphysics scheme instead of WSM6, and the basic Kain-Fritsch cumulus parameterization instead of the newer Multiscale Kain-Fritsch cumulus scheme. The WRF configuration in Table 2-1: *2012 HGB WRF Configuration* will be referred to as the SIP configuration. The SIP configuration will be compared to the Alternate configuration for a June 2012 evaluation.

For wind speed in June 2012, the alternate WRF configuration looks qualitatively better due to a smaller diurnal wind speed bias in Figure 4-18: *June 2012 HGB Wind Speed Time Series using SIP Configuration* and Figure 4-19: *June 2012 HGB Wind Speed Time Series using Alternate Configuration*. On the other hand, the scatter plots show that the SIP configuration has better nighttime performance, as shown in Figure 4-20: *June 2012 HGB Wind Speed Scatter Plot using SIP Configuration* and Figure 4-21: *June 2012 HGB Wind Speed Scatter Plots using Alternate Configuration*. Previous TCEQ meteorological modeling has had nocturnal wind speed biases and the SIP configuration has improved in that regard. Both WRF configurations perform well for a wind speed metric of average error less than 2 m/s.

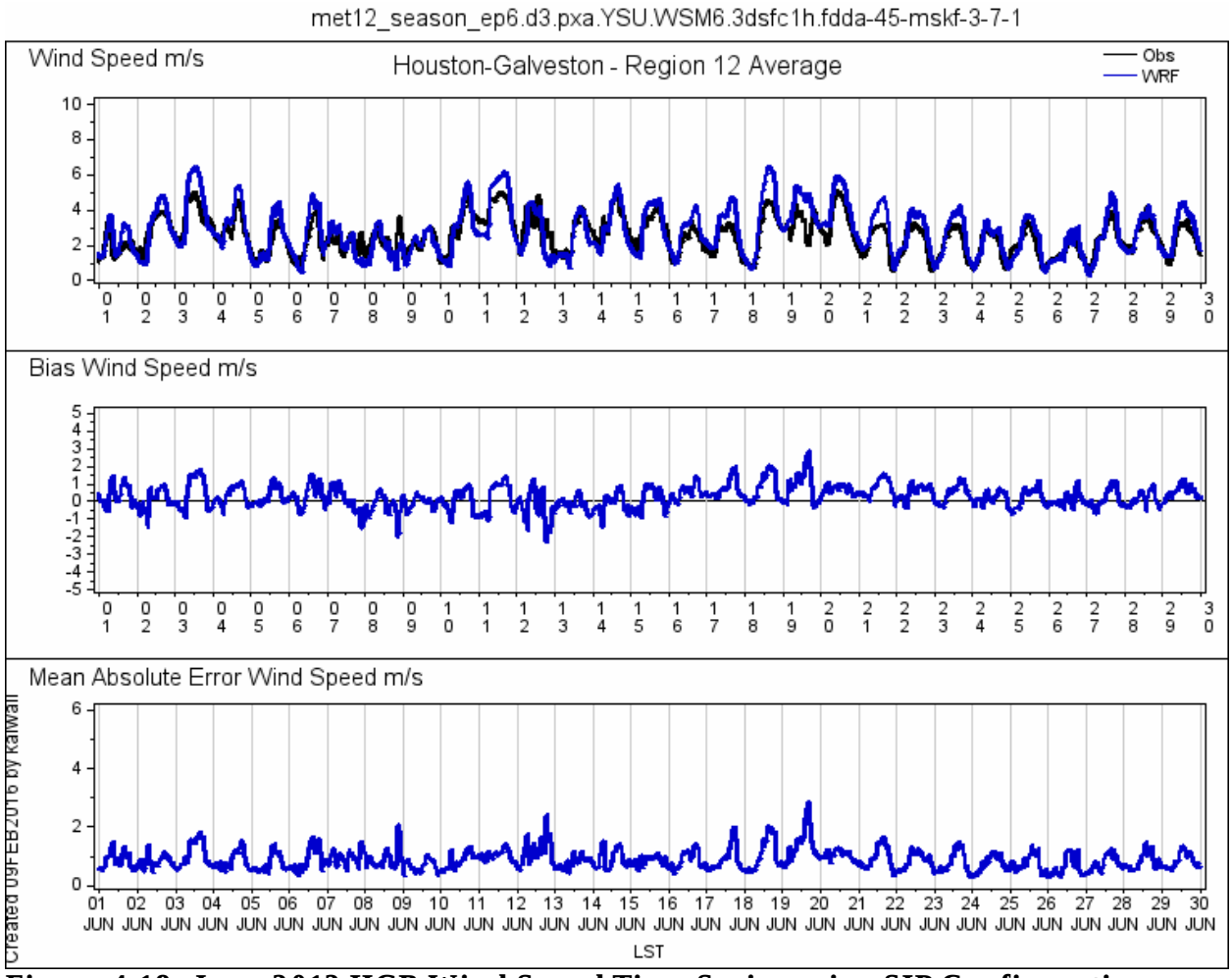

Figure 4-18: June 2012 HGB Wind Speed Time Series using SIP Configuration

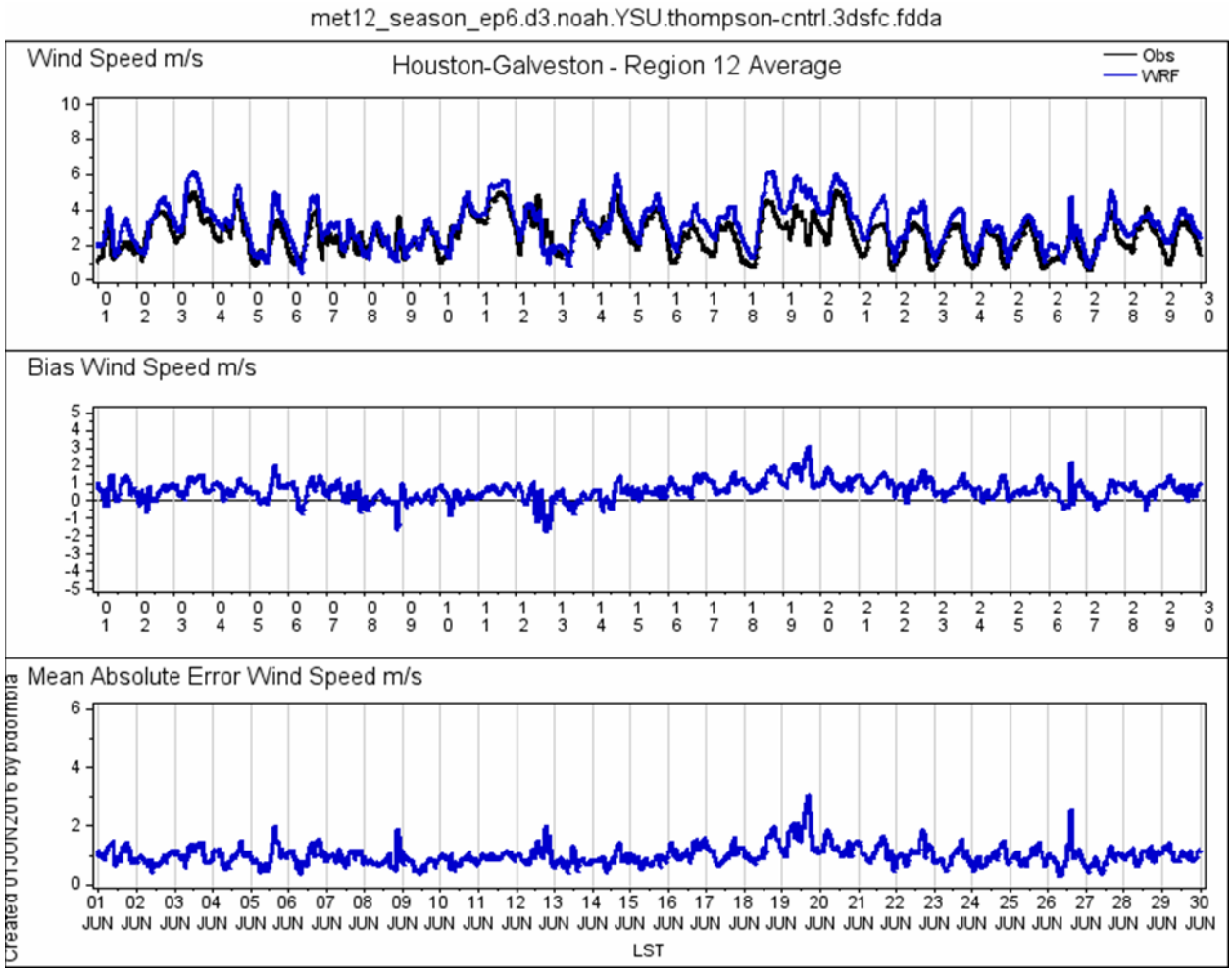

Figure 4-19: June 2012 HGB Wind Speed Time Series using Alternate Configuration

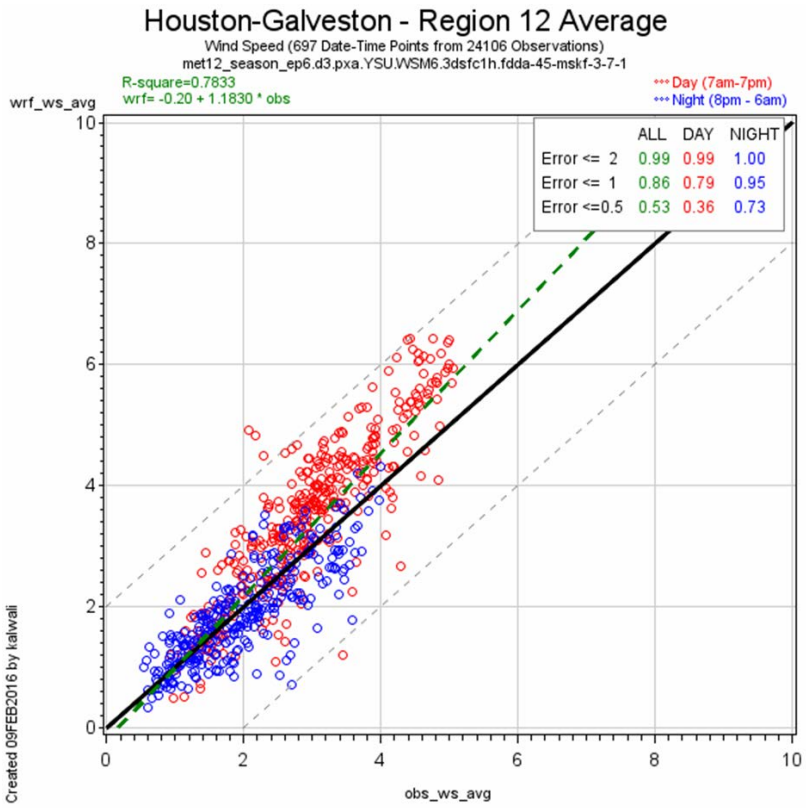

Figure 4-20: June 2012 HGB Wind Speed Scatter Plot using SIP Configuration

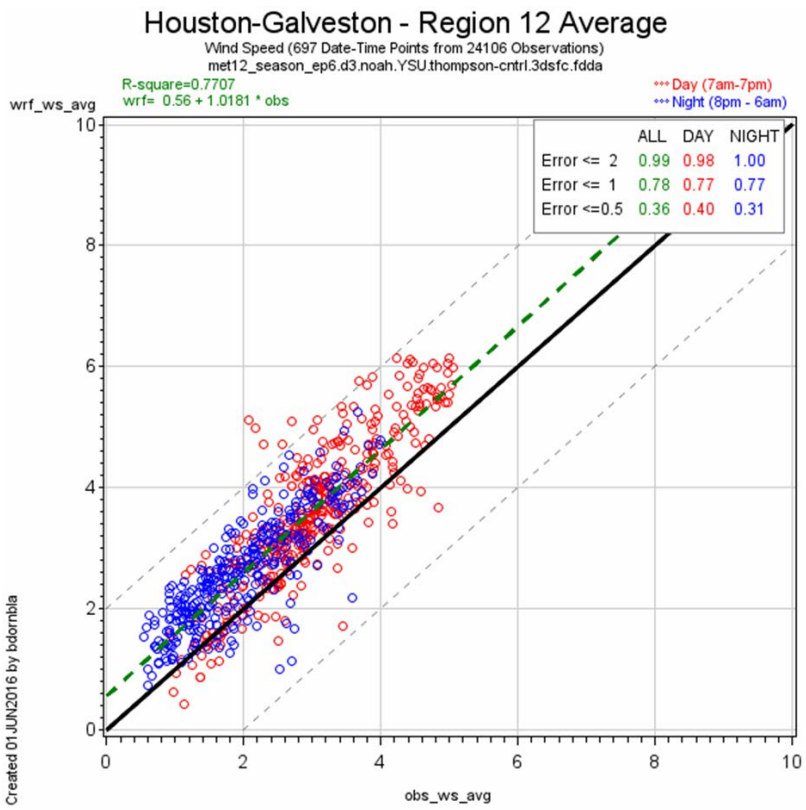

Figure 4-21: June 2012 HGB Wind Speed Scatter Plots using Alternate Configuration

Relative humidity can help assess low level mixing. Both WRF configurations use the same YSU PBL parameterization. However, the choice of LSM modifies the surface fluxes passed to the YSU scheme. Figure 4-22: *June 2012 HGB Humidity for WRF SIP Configuration (top) and WRF Alternate Configuration (bottom)* indicates that the use of the NOAH LSM provides better performance during both daytime and nighttime hours than the PX LSM. However, the HGB area had data at only three sites during June 2012, so this metric carries less weight for evaluation than wind speed, wind direction, or temperature.

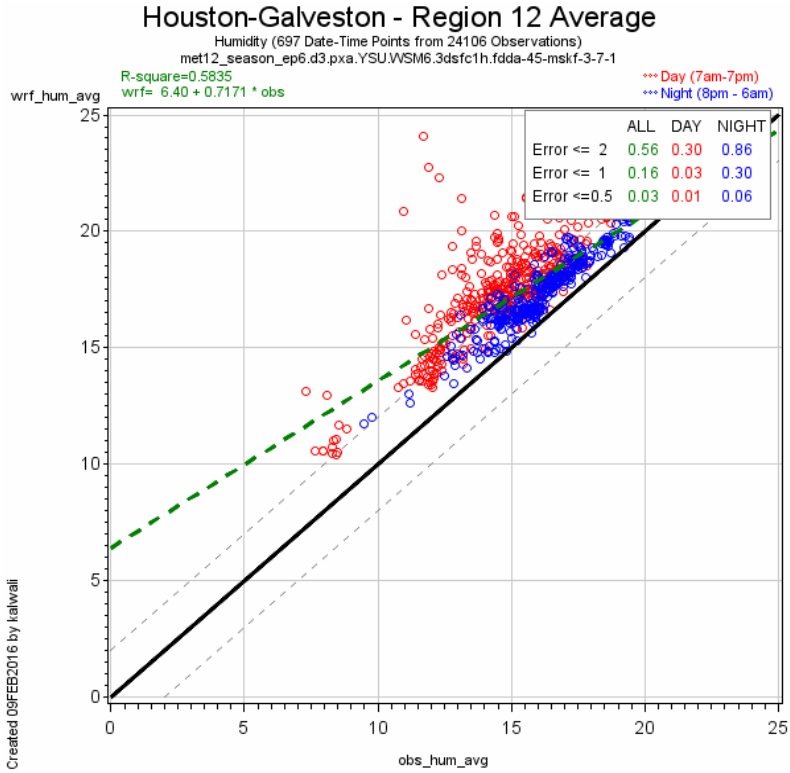

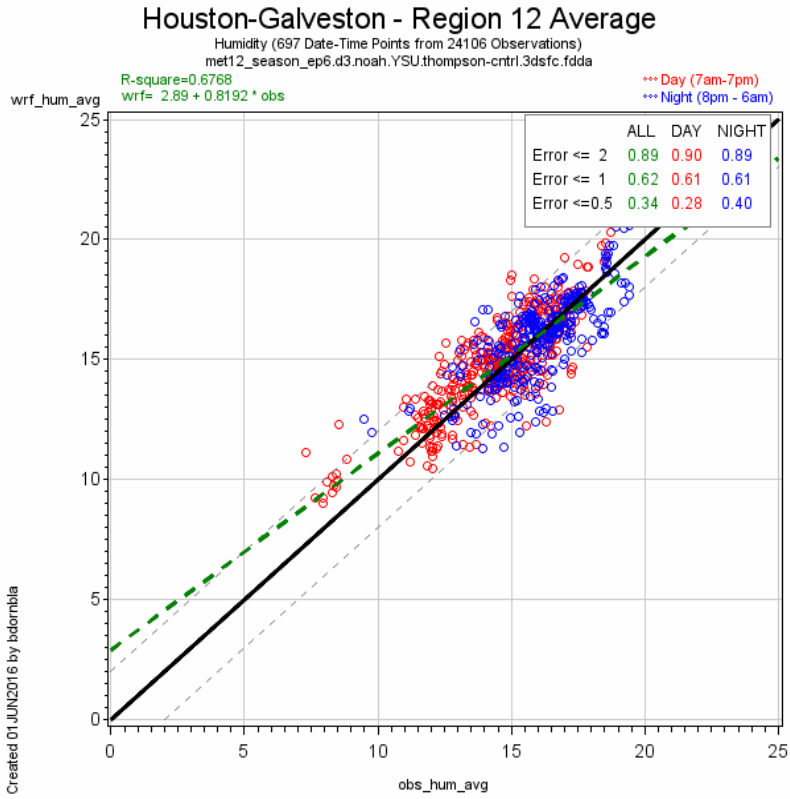

Figure 4-22: June 2012 HGB Humidity for WRF SIP Configuration (top) and WRF Alternate Configuration (bottom)

The effect of the alternate WRF configuration choices on modeled clouds is shown in Figure 4-23: *June 26, 2012: 2pm WRF Maximum Cloud Fraction for Alternate WRF Configuration* and Figure 4-24: *June 26, 2012: 2 pm WRF Shortwave Radiative Flux Performance for Alternate WRF Configuration*. For comparison to the SIP configuration, refer to Figure 3-5: *June 26, 2012: 2 pm WRF Maximum Cloud Fraction* and Figure 3-6: *June 26, 2012: 2 pm WRF Shortwave Radiative Flux Performance*, respectively. The alternate selection of NOAH LSM, moisture microphysics, and the use of the Kain-Fritsch cumulus parameterization produced less cloud cover for this hour and many others throughout June.

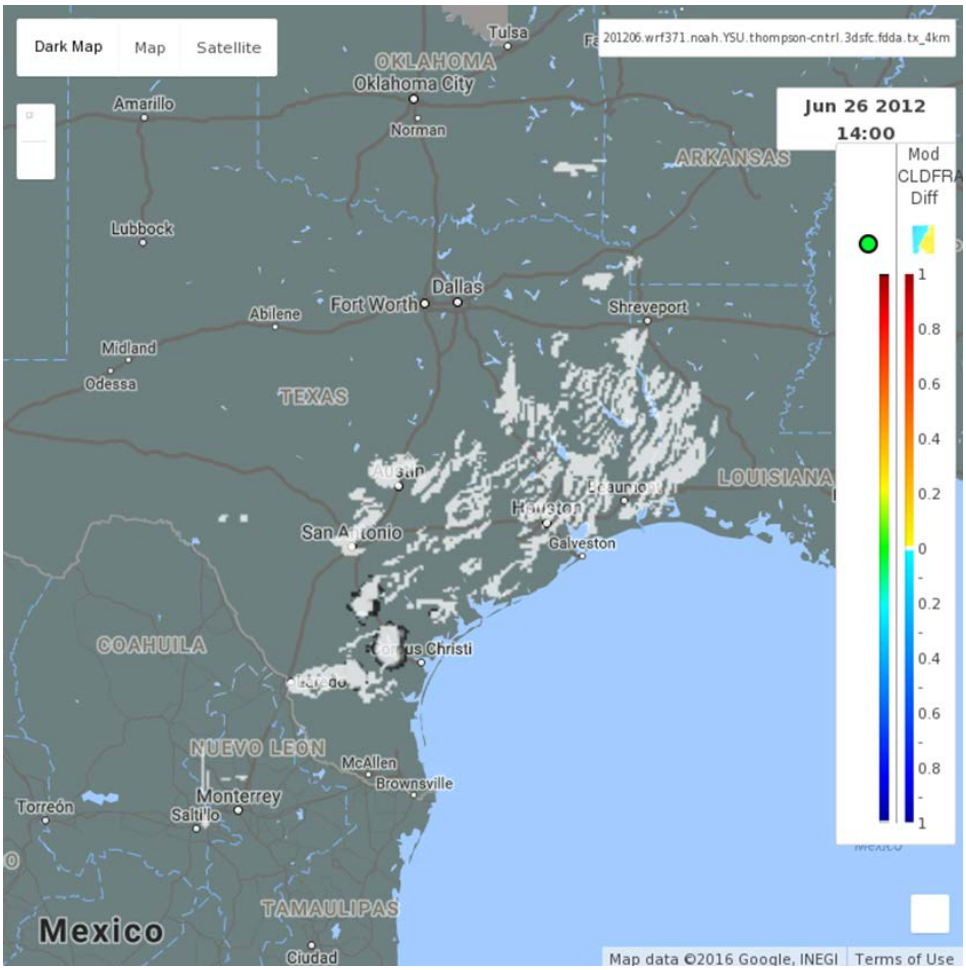

Figure 4-23: June 26, 2012: 2pm WRF Maximum Cloud Fraction for Alternate WRF Configuration

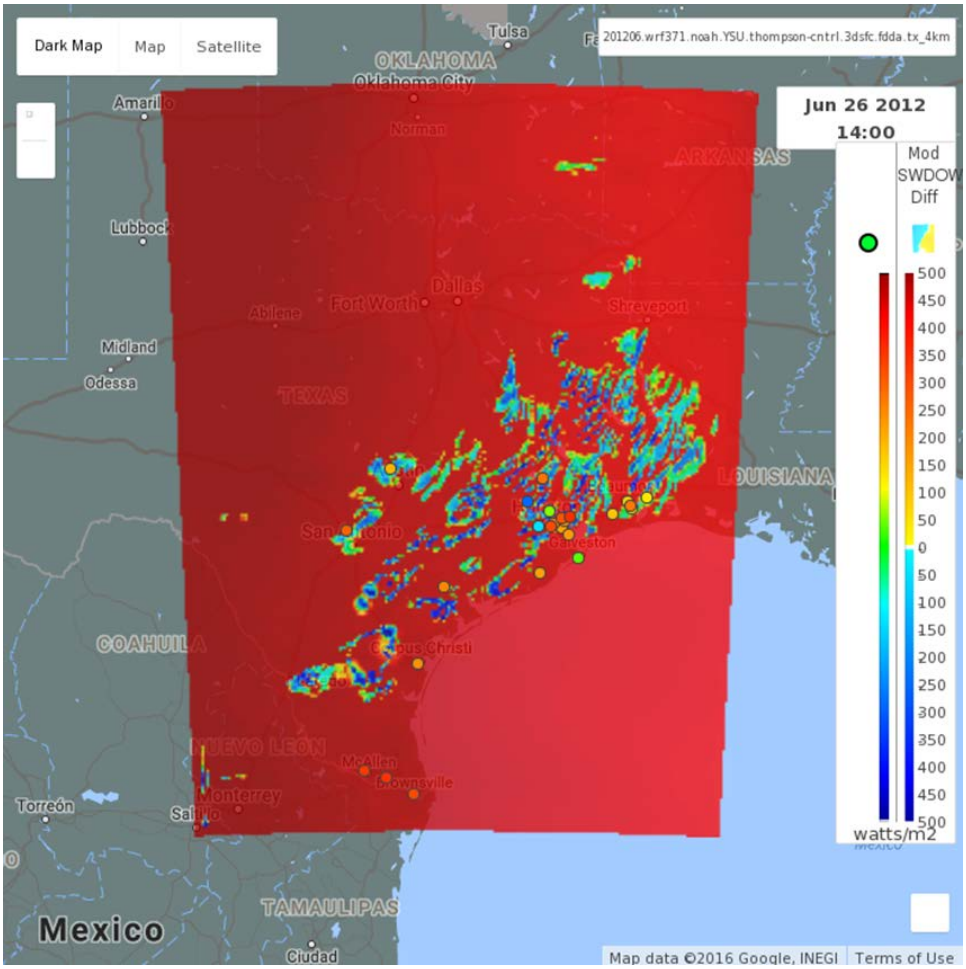

Figure 4-24: June 26, 2012: 2 pm WRF Shortwave Radiative Flux Performance for Alternate WRF Configuration

The interplay between LSM, PBL parameterizations, and cumulus parameterizations is not well understood. Investigating the sensitivity of cloud formation to choice of LSM and improvements in model physics remains an important aspect of future meteorological modeling work.

4.4 July 2012 Episode Performance Evaluation

There were no eight-hour ozone exceedance days in July 2012. The HGB area frequently has lower ozone concentrations when clean air flows from the Gulf of Mexico, which occurred in July 2012. Figure 4-25: *July 2012 HGB Wind Direction Time Series* shows generally southerly winds with some periods of southeasterly to westerly winds. Figure 4-26: *July 2012 HGB* shows that wind speeds during July were frequently close to 2 m/s. In addition, as seen in Figure 4-27: *July 2012 HGB Temperature Time Series*, cooler than average temperatures were associated with above average precipitation and generally cloudy conditions along the Texas coast (National Oceanic and Atmospheric Administration (NOAA), 2012). While slow wind speeds are conducive to ozone formation, the consistent southerly winds and cloudy conditions limited ozone concentrations.

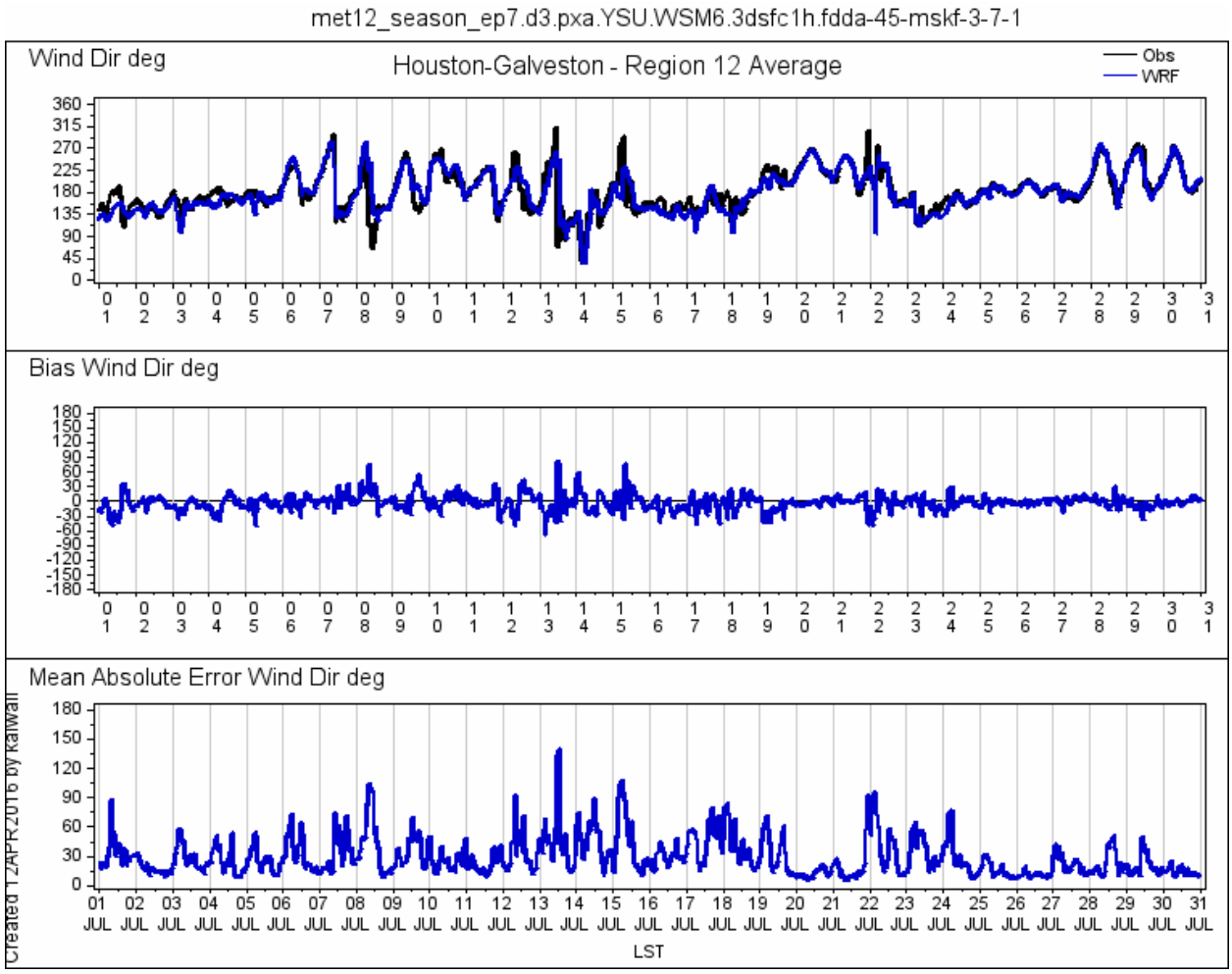

Figure 4-25: July 2012 HGB Wind Direction Time Series

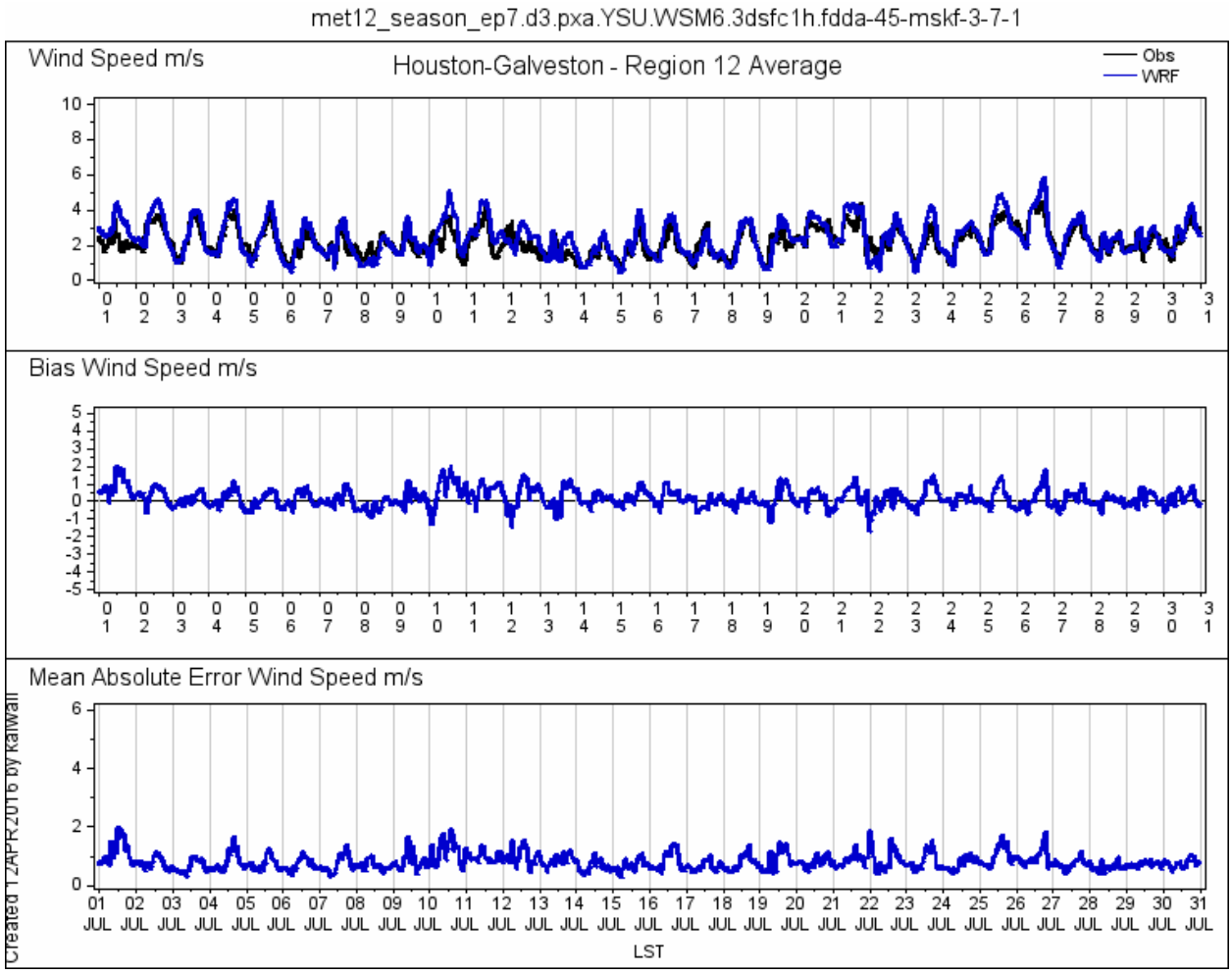

Figure 4-26: July 2012 HGB Wind Speed Time Series

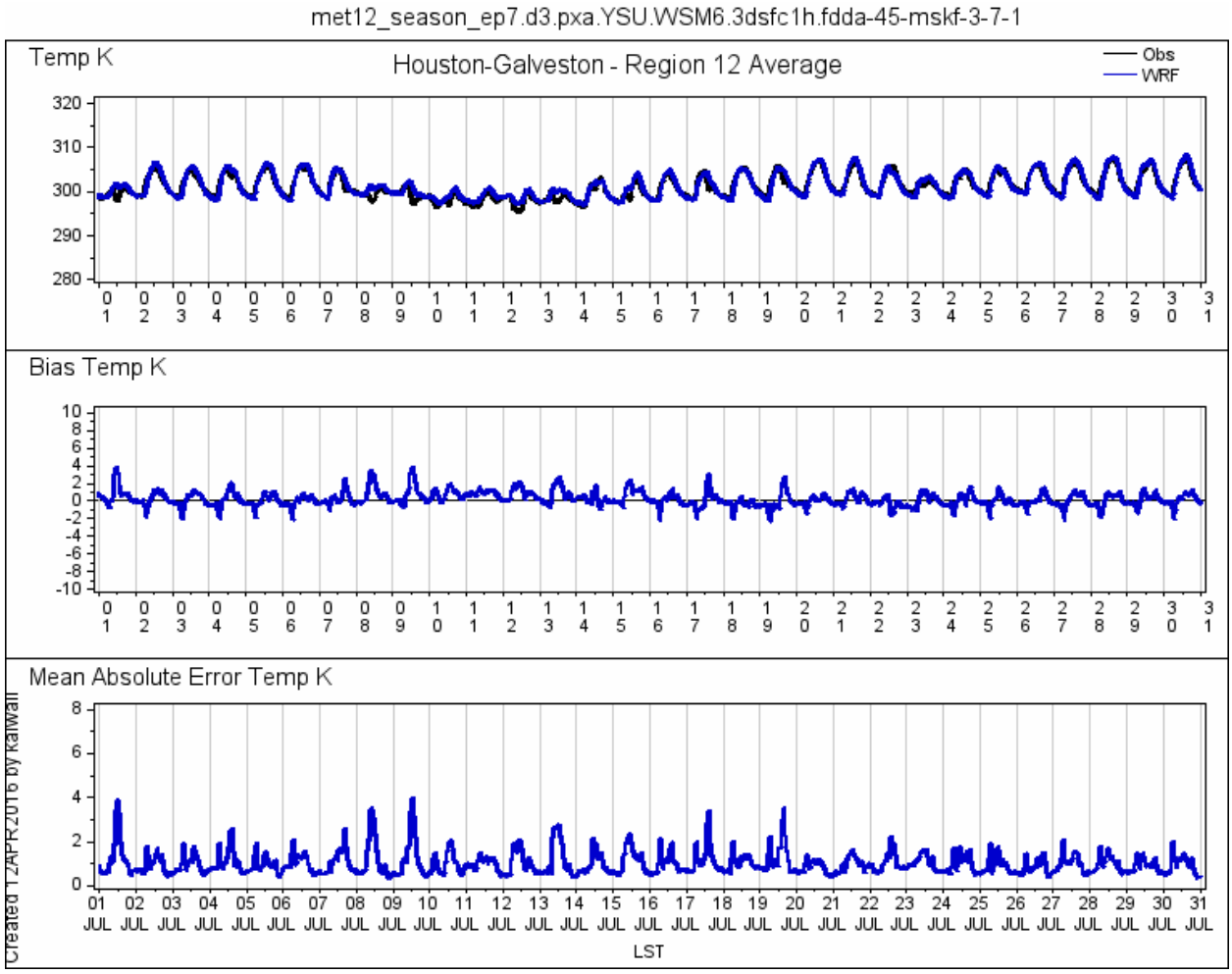

Figure 4-27: July 2012 HGB Temperature Time Series

4.5 August 2012 HGB Episode Performance Evaluation

August 2012 had significant eight-hour exceedances on August 6 and 7. The highest eight-hour ozone was 98.2 ppb on August 20. The wind direction performance for the region, shown in Figure 4-28: *August 2012 HGB Wind Direction Time Series*, was very good with respect to bias. The evolution of wind directions for August 7 and 20 look remarkably similar in Figure 4-28. The absolute errors for these days was associated with a combination of light wind hours and sea breeze interactions with veering winds.

Unlike previously discussed days in May and June, stagnation arrives early on August 7. These features result in a scatter plot for wind direction, Figure 4-29: *August 7, 2012 HGB Wind Direction Scatter Plot*, quite different from earlier scatter plots for selected days in May and June. On August 7, early morning southerly winds become very weak and calm by six or seven am. There is still an offshore wind. Winds remain light and disorganized until noon when the sea breeze becomes established and steady from the southeast. Figure 4-30: *August 7, 2012 HGB Wind Speed Scatter Plot* shows that early morning and morning winds are the lightest of the day.

August 20 begins with southerly winds that veer clockwise strongly to the northwest and persist until early in the afternoon. The sea breeze arrives in mid-afternoon. This feature is partially

captured in Figure 4-31: *August 20, 2012 4 pm Surface Wind Map*. Modeled wind directions have good performance in the early morning and afternoon, but as winds calm later in the afternoon, as shown in Figure 4-33: *August 20, 2012 HGB Wind Speed Scatter Plot*, wind direction performance becomes poor as shown in Figure 4-32: *August 20, 2012 HGB Wind Direction Scatter Plot*.

Wind speeds tended to be light during August, and Figure 4-34: *August 2012 HGB Wind Speed Time Series* shows that WRF maintained low biases and absolute errors throughout the month. Temperature performance had smaller diurnal biases than previous months, as shown in Figure 4-35: *August 2012 HGB Temperature Time Series*, even though many days had variable clouds in east Texas.

August 20 was largely free of clouds and there was greater available shortwave radiation as seen in Figure 4-36: *August 20, 2012: 2 pm WRF Shortwave Radiative Flux Performance* as compared to Figure 4-37: *August 7, 2012: 2 pm WRF Shortwave Radiative Flux Performance*. Both days show significant ozone, but among the meteorological variables, small differences in wind speed and total solar radiation may impact the final daily modeled averages. As on some of the other high ozone days during the HGB 2012 modeling episode, the modeled downward solar radiation is spatially variable and under-predicts observed solar radiation in Houston at mid-day and afternoon hours. This may impact modeled hourly ozone values at particular sites in Houston.

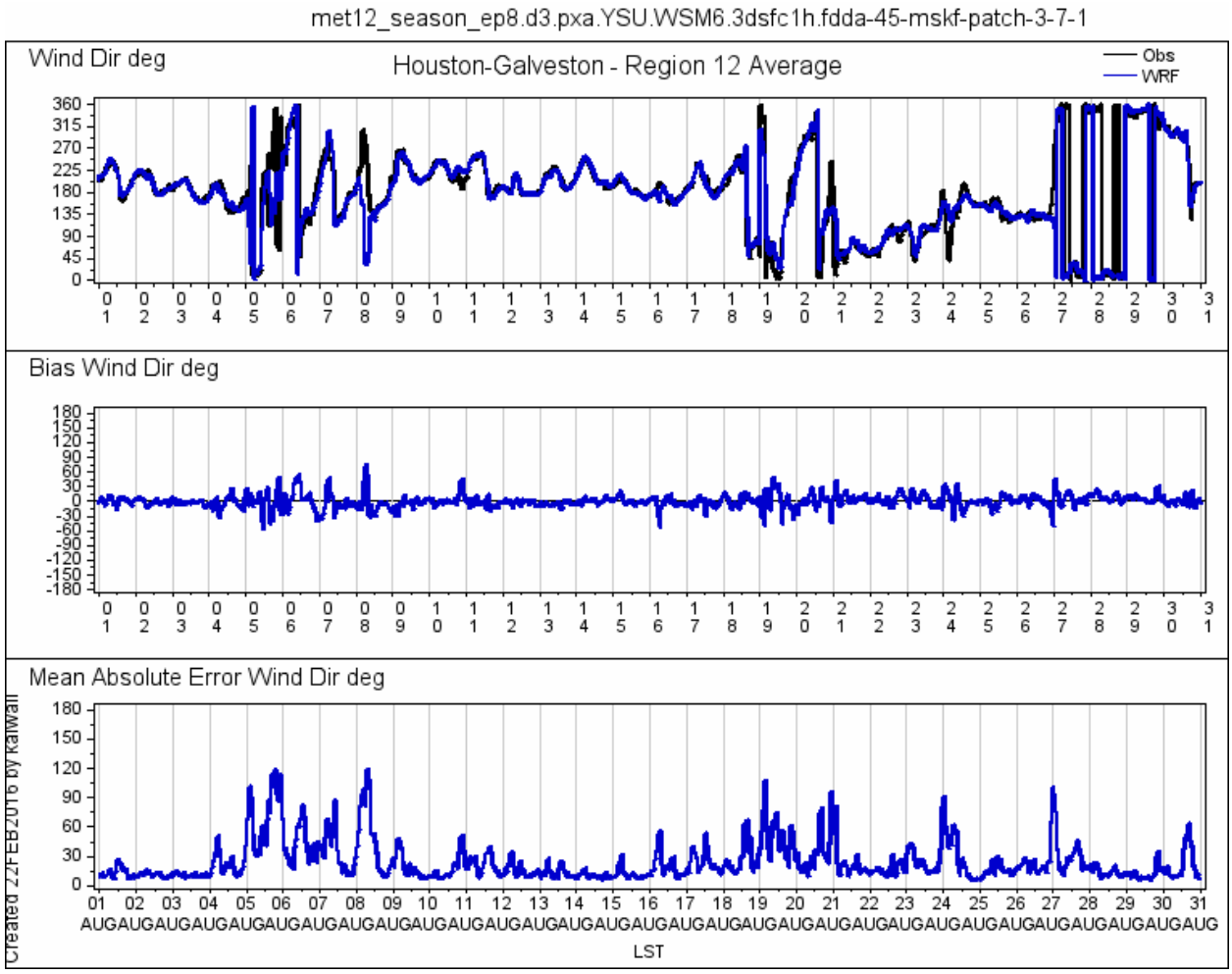

Figure 4-28: August 2012 HGB Wind Direction Time Series

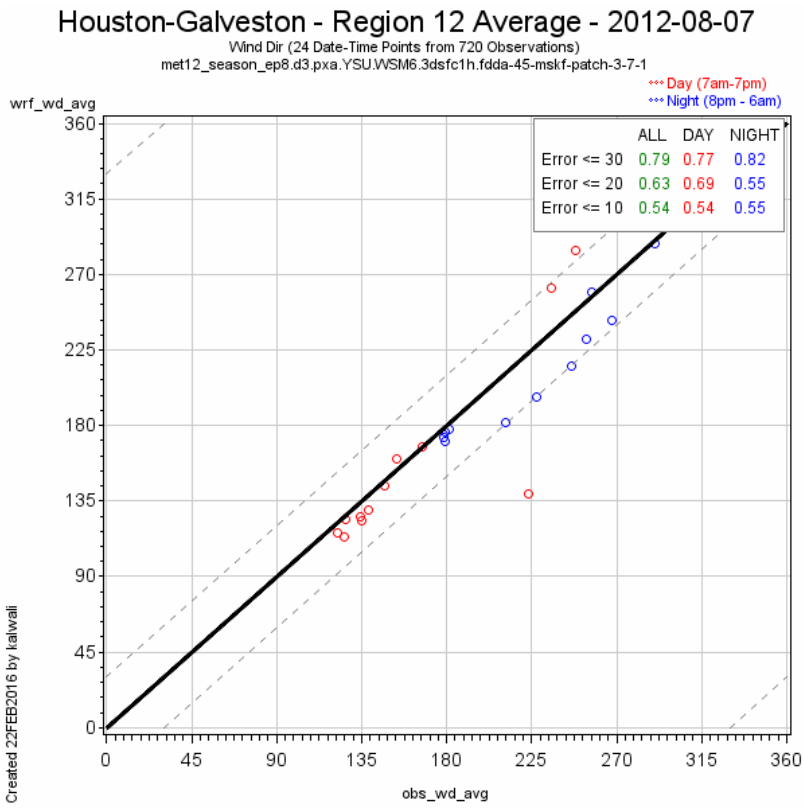

Figure 4-29: August 7, 2012 HGB Wind Direction Scatter Plot

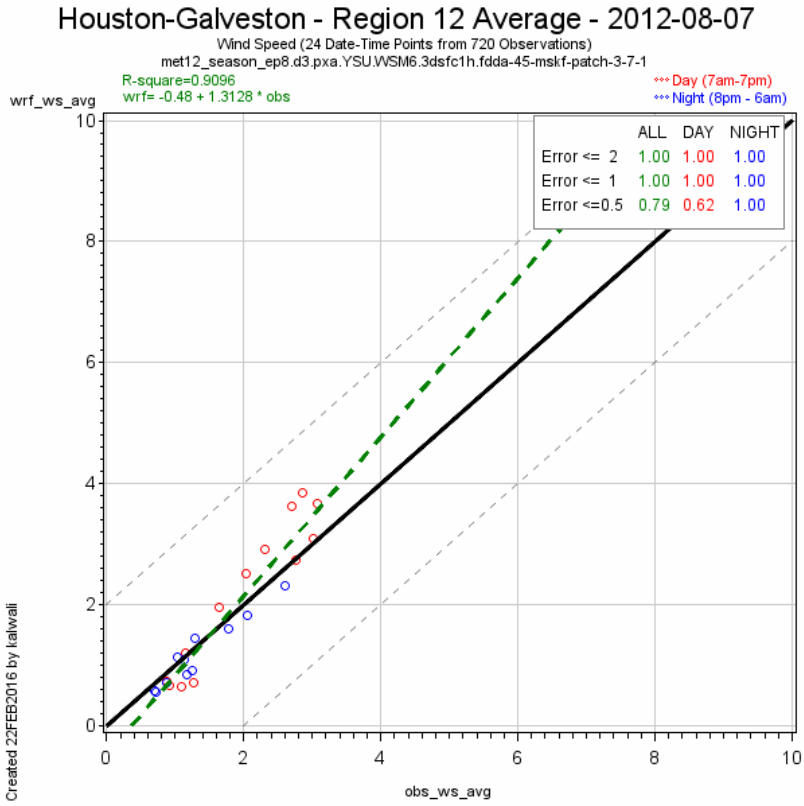

Figure 4-30: August 7, 2012 HGB Wind Speed Scatter Plot

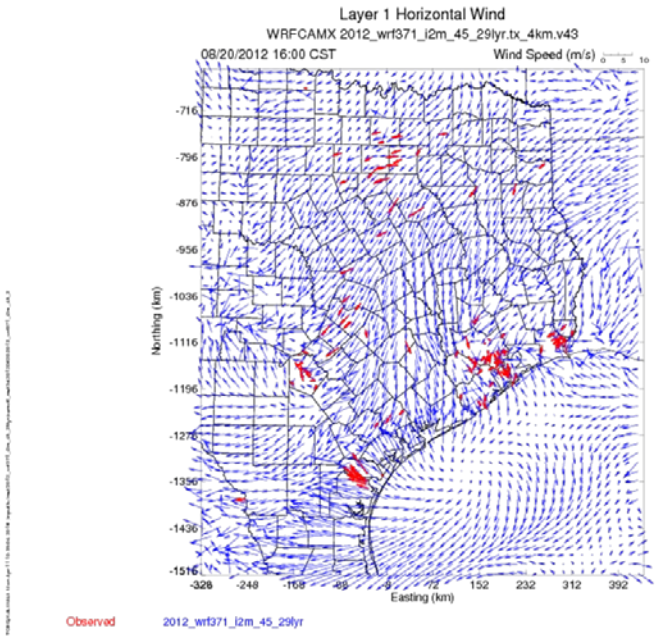

Figure 4-31: August 20, 2012 4 pm Surface Wind Map

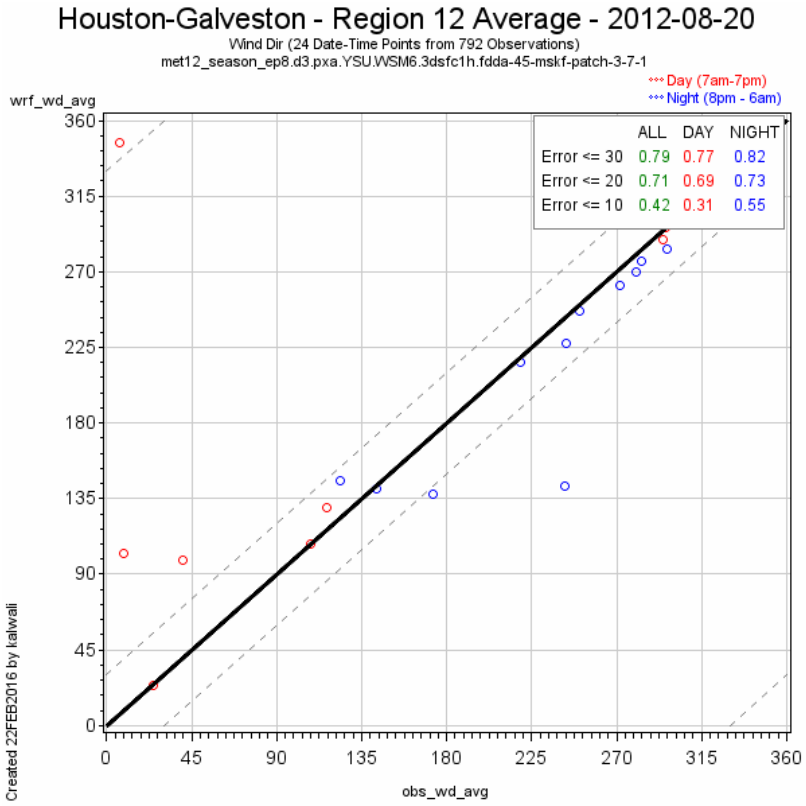

Figure 4-32: August 20, 2012 HGB Wind Direction Scatter Plot

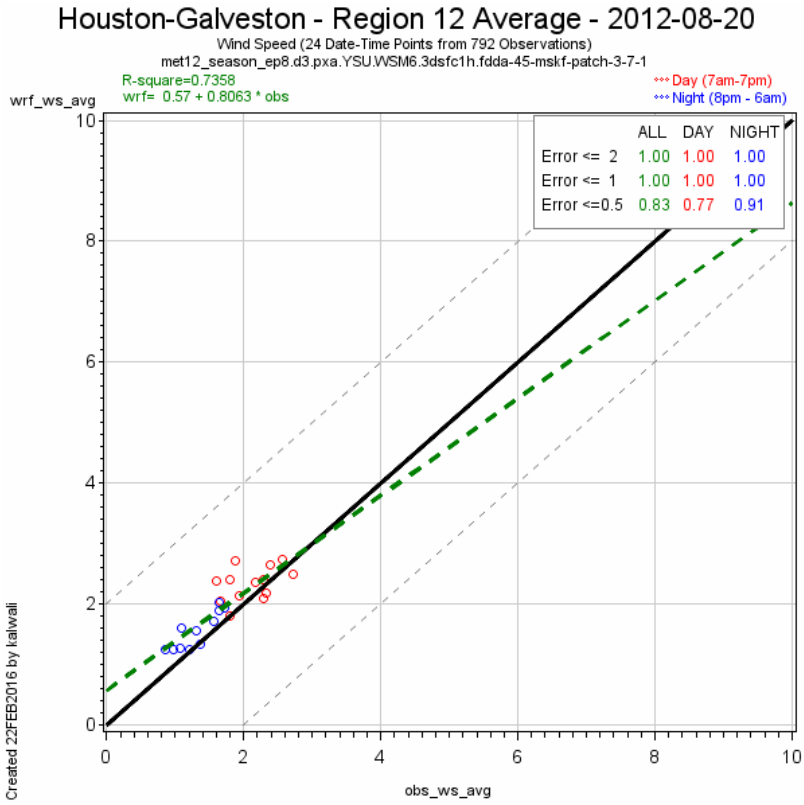

Figure 4-33: August 20, 2012 HGB Wind Speed Scatter Plot

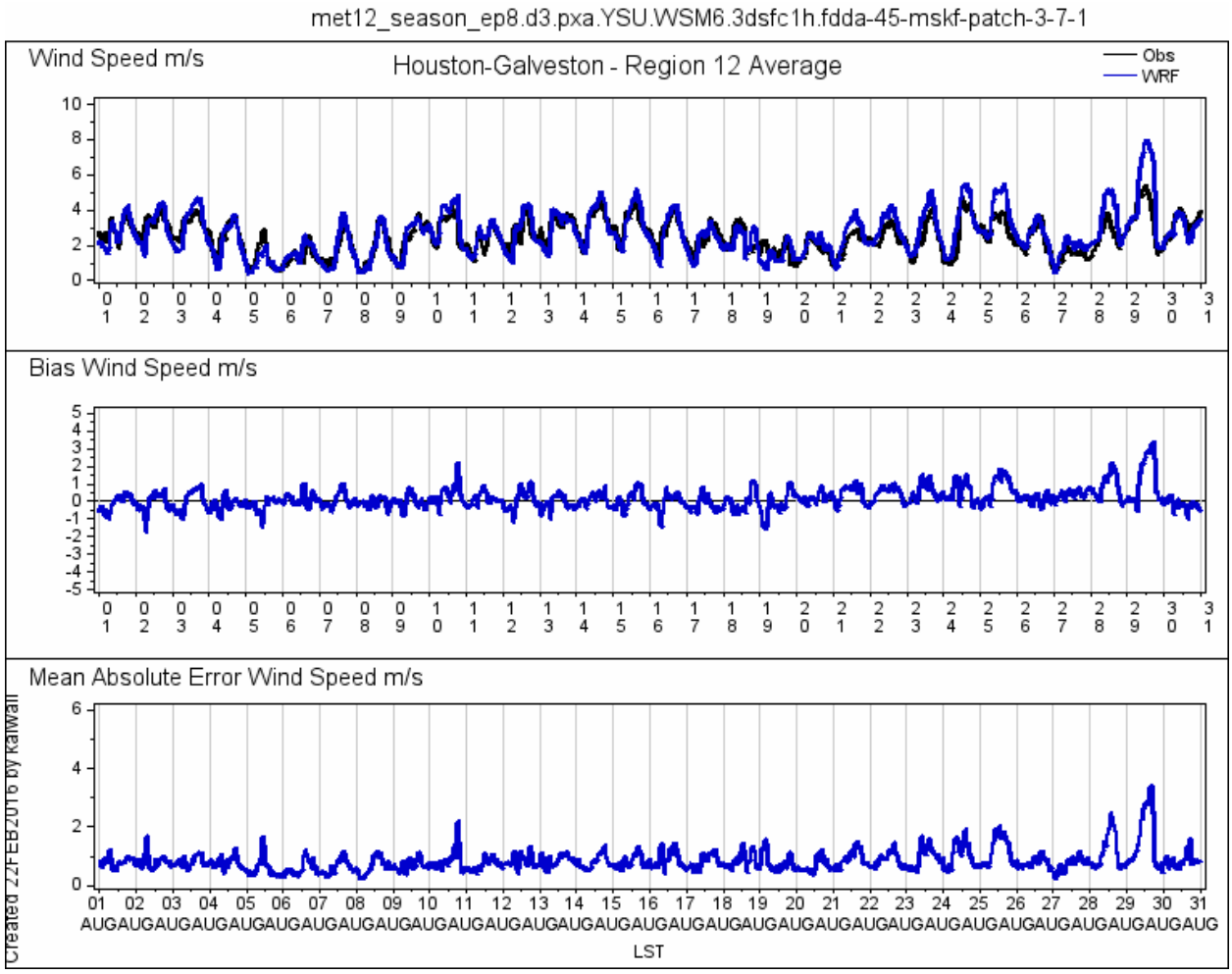

Figure 4-34: August 2012 HGB Wind Speed Time Series

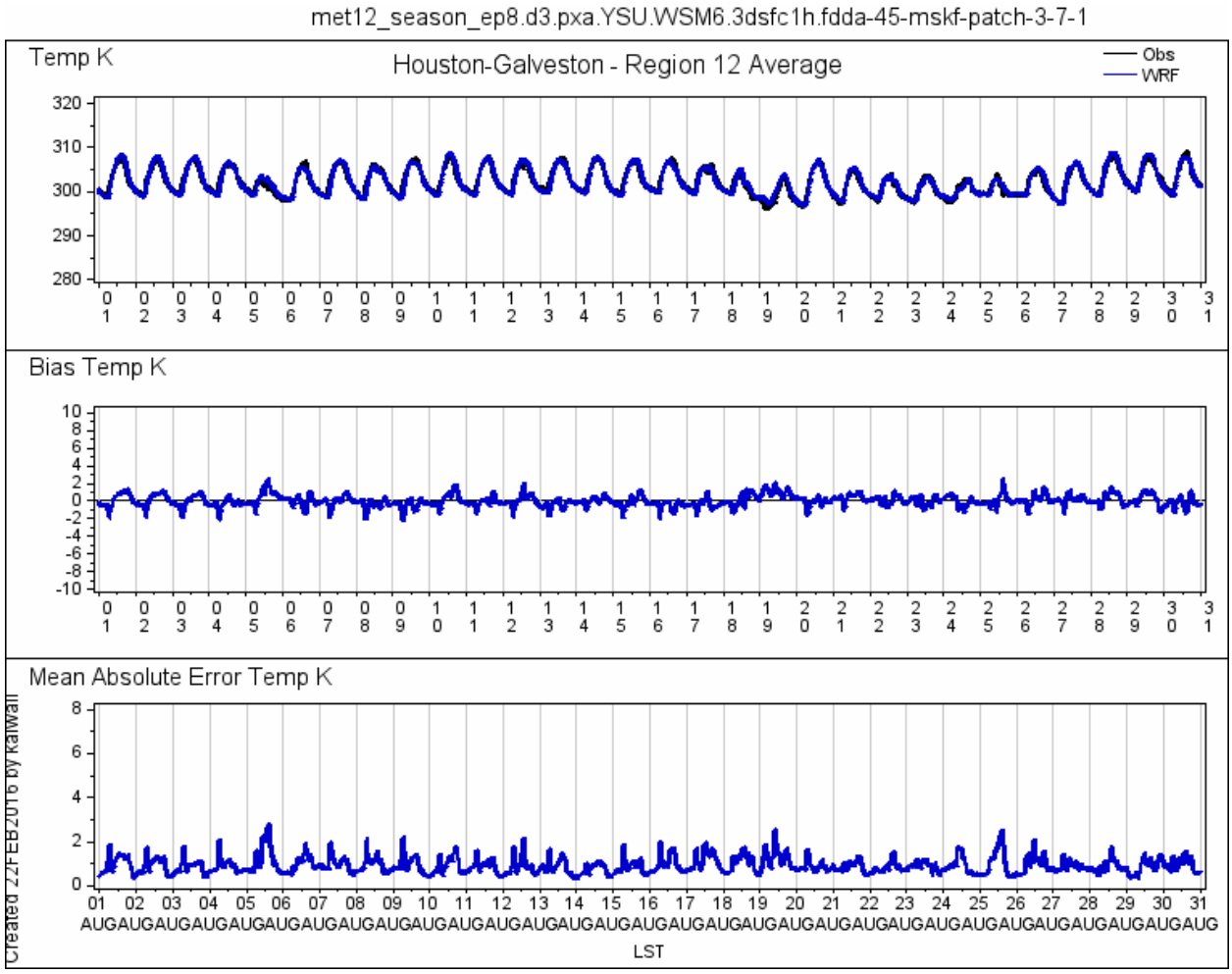

Figure 4-35: August 2012 HGB Temperature Time Series

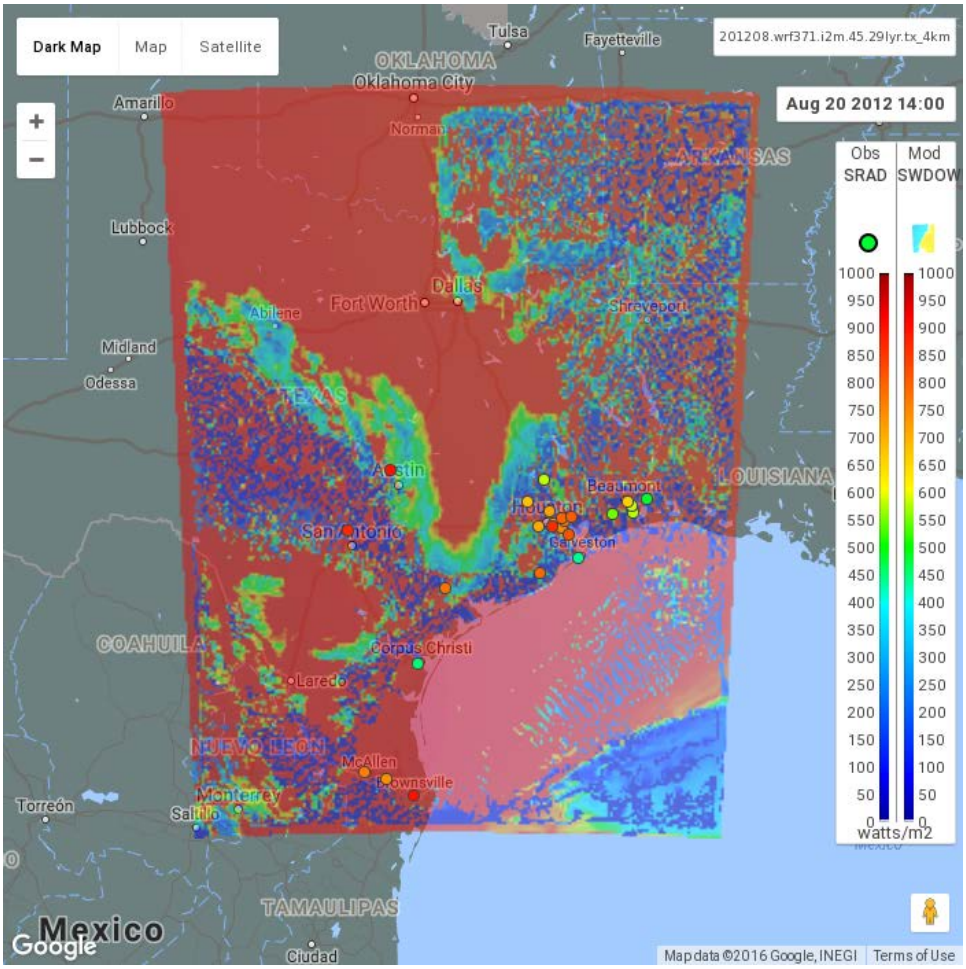

Figure 4-36: August 20, 2012: 2 pm WRF Shortwave Radiative Flux Performance

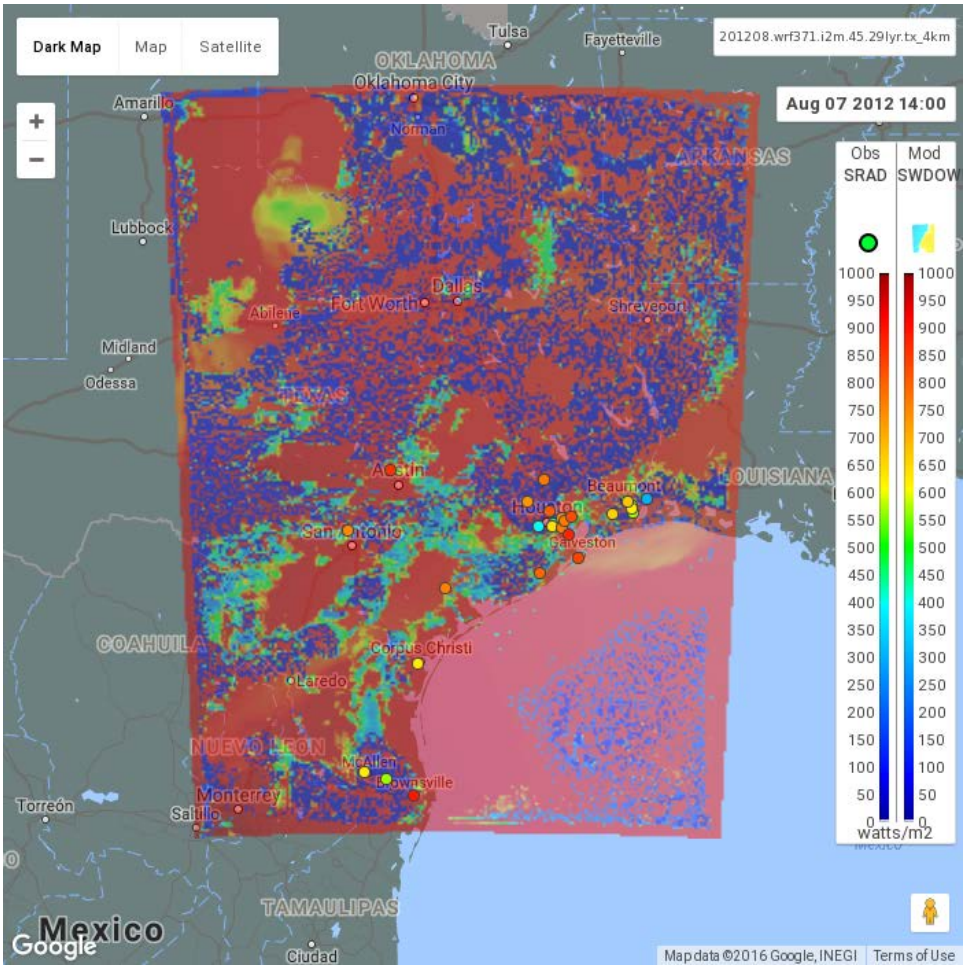

Figure 4-37: August 7, 2012: 2 pm WRF Shortwave Radiative Flux Performance

Overall performance is summarized in Table 4-3: *August 2012 HGB Meteorological Modeling Percent Accuracy*.

Table 4-3: August 2012 HGB Meteorological Modeling Percent Accuracy

HGB Area	Wind Direction (°) Error ≤ 30 / 20 / 10	Wind Speed (m/s) Error ≤ 2 / 1 / 0.5	Temperature (°C) Error ≤ 2 / 1 / 0.5
Region 12 Average	89 / 83 / 65	98 /91 / 69	99 / 86 / 61
Manvel Croix	70 / 59 / 35	95 / 79 / 48	92 /67 / 43
Deer Park	78 / 65 /42	95 / 79 / 51	89 / 59/ 28
Clinton Drive	63 / 41 / 20	92 / 65 / 39	93 / 62 / 32
Channelview	74 / 62 / 36	95 / 73 /46	83 / 44 / 22
Aldine	71 / 58 / 34	95 / 78 / 50	97 / 77 / 46
Bayland Park	80 / 68 / 43	97 / 80 / 52	94 / 69 / 44
Northwest Harris Co.	71 / 60 / 35	98 / 80 / 47	96 / 79 / 47
Conroe	66 / 53 / 32	95 / 70 / 39	78 / 48 / 27

4.6 September 2012 HGB Episode Performance Evaluation

The HGB region can have high ozone days extending into September. The tenth highest eight-hour ozone day for the HGB 2012 modeling episode occurred on September 2o, again at Manvel Croix Park, with a value of 87.8 ppb. Other notable days were September 22 and 23 with reported values of 82.8 and 82.0 ppb, respectively. As shown in Figure 4-38: *September 2012 HGB Wind Direction Time Series*, September 3 began with easterly flow. Winds shifted to the northeast and became calm around 10 am and later shifted to the southeast and strengthened until late in the afternoon when winds calmed again. These features are partially captured in Figure 4-40: *September 20, 2012 HGB Wind Direction Scatter Plot* and Figure 4-41: *September 20, 2012 HGB Wind Speed Scatter Plot*. The next three days began with northerly flow that veered clockwise from easterly to southerly flow. Winds were very light during this entire period, and there were no significant clouds to complicate the meteorology. As in other months, wind direction errors were most pronounced near midnight on several days when winds were less than 1 m/s.

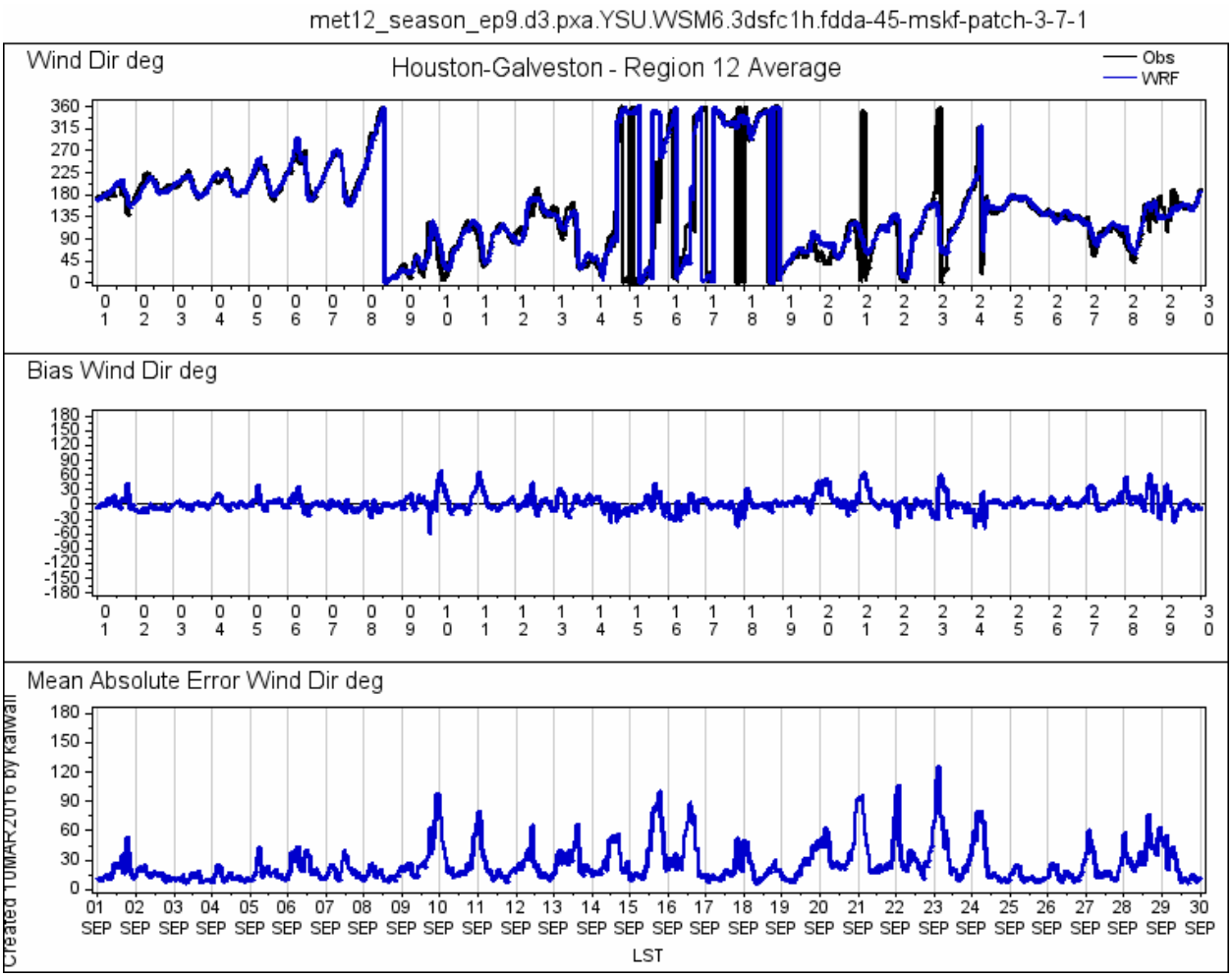

Figure 4-38: September 2012 HGB Wind Direction Time Series

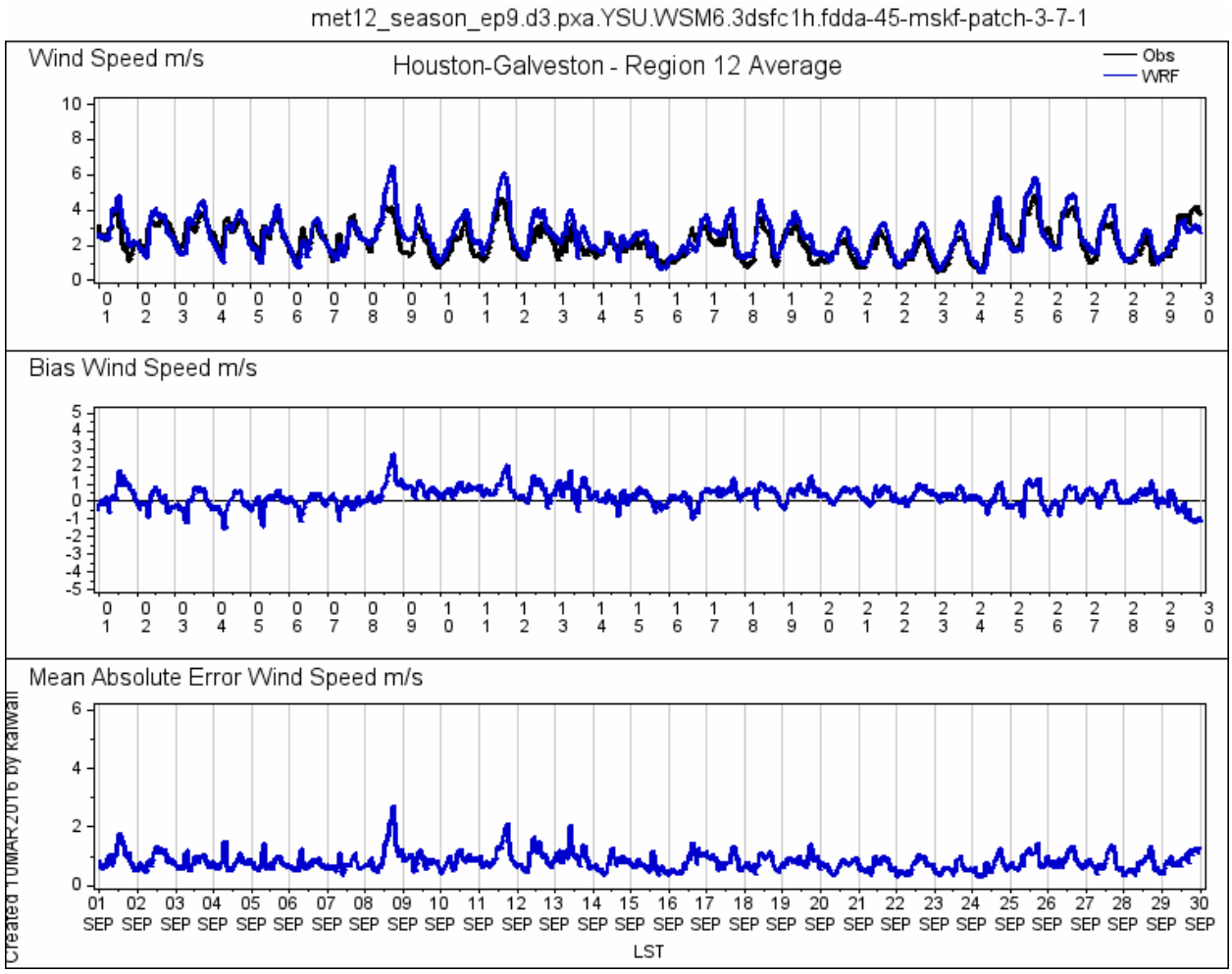

Figure 4-39: September 2012 HGB Wind Speed Time Series

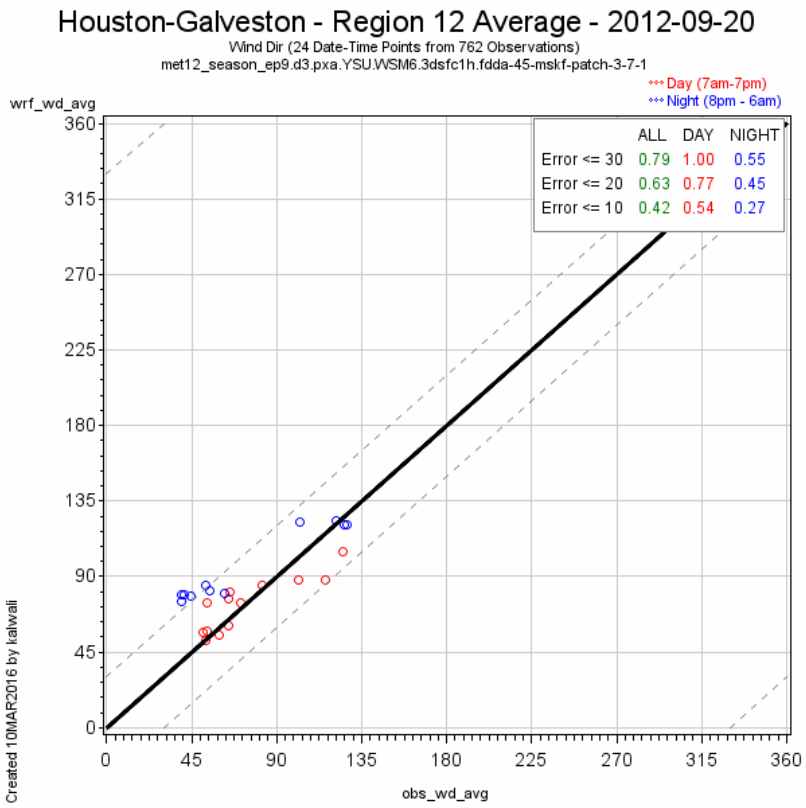

Figure 4-40: September 20, 2012 HGB Wind Direction Scatter Plot

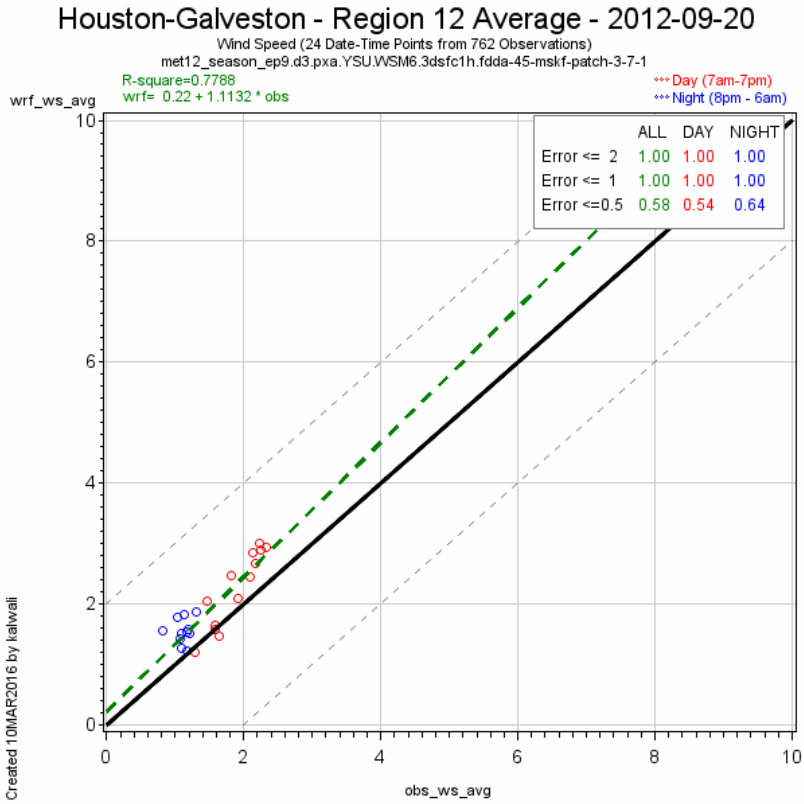

Figure 4-41: September 20, 2012 HGB Wind Speed Scatter Plot

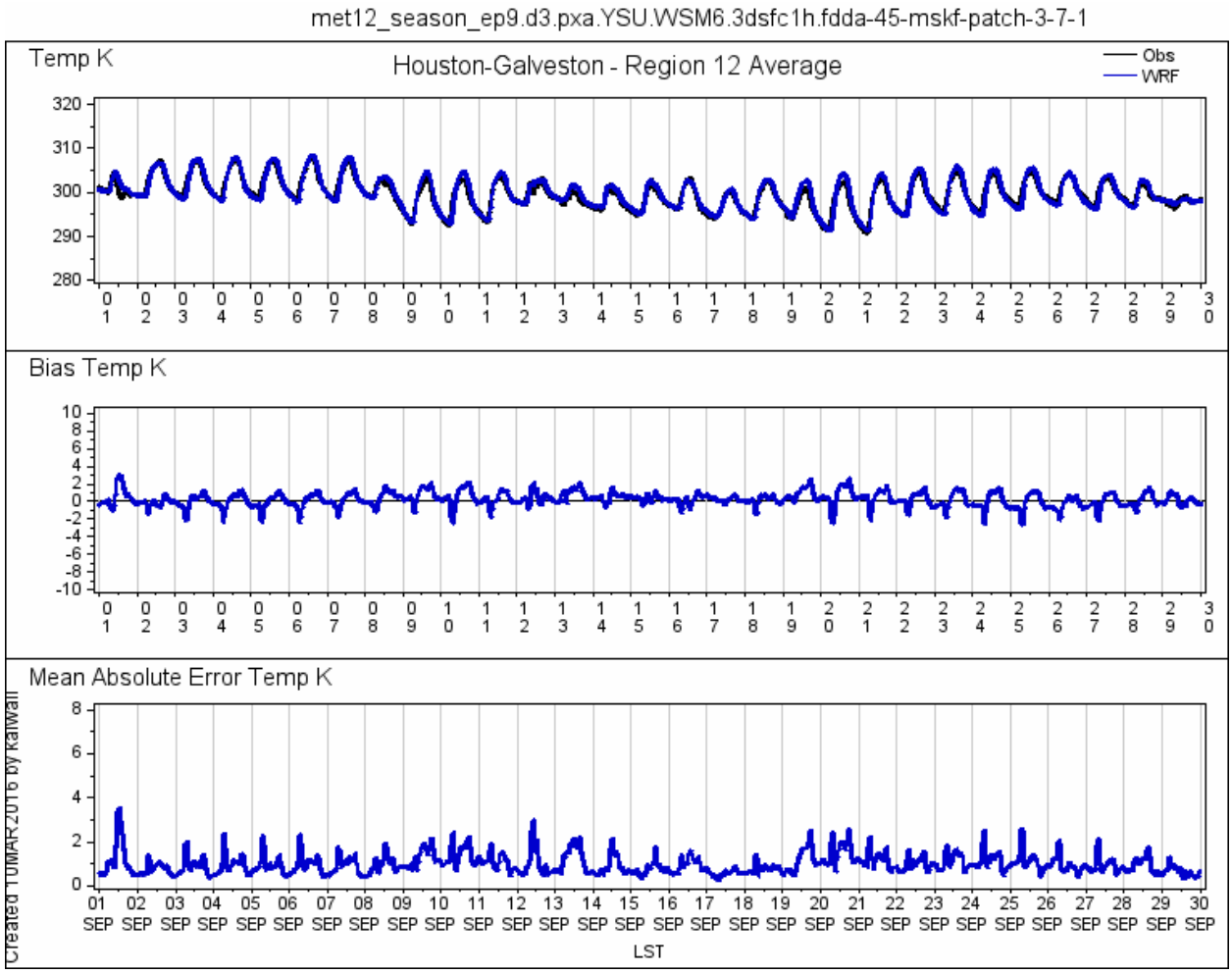

Figure 4-42: September 2012 HGB Temperature Time Series

Overall performance is summarized in Table 4-4: *September 2012 HGB Meteorological Modeling Percent Accuracy*.

Table 4-4: September 2012 HGB Meteorological Modeling Percent Accuracy

HGB Area	Wind Direction (°) Error ≤ 30 / 20 / 10	Wind Speed (m/s) Error ≤ 2 / 1 / 0.5	Temperature (°C) Error ≤ 2 / 1 / 0.5
Region 12 Average	90 / 83 / 63	99 /91 / 57	97 / 76 / 47
Manvel Croix	76 / 63 / 36	97 / 78 / 47	84 /58 / 37
Deer Park	72 / 59 /37	97 / 68 / 41	83 / 52/ 24
Clinton Drive	66 / 45 / 21	93 / 66 / 34	87 / 52 / 25
Channelview	72 / 59 / 35	97 / 78 /47	82 / 40 / 19
Aldine	69 / 53 / 32	97 / 81 / 44	94 / 72 / 45
Bayland Park	78 / 67 / 43	98 / 87 / 58	91 / 68 / 39
Northwest Harris Co.	66 / 54 / 32	98 / 79 / 47	96 / 75 / 47
Conroe	59 / 47 / 29	96 / 78 / 47	72 / 47 / 26

4.7 Conclusions

WRF modeling of the HGB 2012 meteorological season provided consistently good area-wide performance across several metrics. In addition to traditional metrics of wind speed, wind direction, and temperature, WRF shortwave radiation flux values were consistent with observed cloud placement. The spatial variability of the modeled shortwave radiation flux were similar to the same variability in the surface data. Mesoscale features such as the evolution of veering surface winds and onset of sea breezes were well characterized in the WRF modeling. This meteorology was considered suitable for input into photochemical modeling.

5. REFERENCES

Biazar, A. P., R. T. McNider, R. White, D. S. Cohan, R. Zhang (2015), Incorporating Space-borne Observations to Improve Biogenic emission Estimates in Texas, Final Report, Texas Air Quality Research Program (AQRP) Project 14-017, http://aqrp.ceer.utexas.edu/projectinfoFY14_15%5C14-017%5C14-017%20Final%20Report.pdf.

Bullock Jr., O. R., K. Alapaty, J. Herwehe, J. Kain (2015), A dynamically Computed Convective Time Scale for the Kain-Fritsch Convective Parameterization Scheme, Mon. Wea. Rev., 143(6), 2105-2120.

Emery, C., E. Tai, and G. Yarwood (2001), Enhanced Meteorological Modeling and Performance Evaluation for Two Texas Ozone Episodes, Final Report to the Texas Natural Resource Conservation Commission under TNRCC Umbrella Contract No. 582-0-31984, Environ International Corporation, Novato, CA.

NOAA (2012), National Oceanic and Atmospheric Administration National Temperature and Precipitation Maps, http://www.ncdc.noaa.gov/sotc/national/201207.

Skamarock, W. C., J. B. Klemp, J. Dudhia, D. O. Gill, D. M. Barker, W. Wang, and J. G. Powers, 2005: A description of the Advanced Research WRF Version 2. NCAR Tech Notes-468+STR.